THE ASTRONOMICAL JOURNAL, 115:708–724, 1998 February

GLOBAL KINEMATICS OF THE GLOBULAR CLUSTER M15[1]

G. A. DRUKIER, S. D. SLAVIN, H. N. COHN, P. M. LUGGER, AND R. C. BERRINGTON
Department of Astronomy, Indiana University, 319 Swain West, Bloomington, IN 47405; drukier@pegasus2.astro.indiana.edu
B. W. MURPHY
Department of Physics and Astronomy, Butler University, 4600 Sunset Avenue, Indianapolis, IN 46208
AND
P. O. SEITZER
Department of Astronomy, University of Michigan, 830 Dennison Building, Ann Arbor, MI 48109
Received 1997 September 24; revised 1997 October 30

ABSTRACT

We present velocities for 230 stars in the outer parts of the globular cluster M15 measured with the Hydra multifiber spectrograph on the 3.5 m WIYN telescope. A new Bayesian technique is used for analyzing the data. The mean velocity of the cluster is -106.9 ± 0.3 km s^{-1}. Rotation with an amplitude of 1.5 ± 0.4 km s^{-1} and a position angle of $125° \pm 19°$ is observed, and a model including rotation is marginally favored over one without rotation. The velocity dispersion decreases from the center out to about 7′ and then appears to increase slightly. This behavior is strikingly different from the continued decline of velocity dispersion with increasing radius that is expected in an isolated cluster. We interpret this as an indication of heating of the outer part of M15 by the Galactic tidal field.

Key words: globular clusters: individual (M15) — methods: statistical

1. INTRODUCTION

1.1. *Theoretical Background*

A full understanding of globular cluster dynamical evolution—including the core-collapse process and its aftermath—requires that global dynamical models be fitted to global data sets. In close analogy with the strong coupling between a stellar core and envelope, there is a strong interaction between the core and halo of a globular cluster. For both stars and clusters, the energy transport rate in the outer parts determines the time-averaged rate of energy generation in the core (Hut et al. 1992). In clusters, star-star gravitational scattering is the energy transport mechanism and hard binaries are the central energy source.

Over the past few years, we have fitted isotropic Fokker-Planck models to the surface density and velocity dispersion profiles of several collapsed-core clusters, including M15 (Grabhorn et al. 1992; Dull et al. 1997), NGC 6624 (Grabhorn et al. 1992), and NGC 6397 (Drukier 1995). We have recently extended our Fokker-Planck approach to the accurate treatment of an anisotropic velocity distribution (Drukier et al. 1997). This will allow us to produce fully global models that include the radial orbit bias that develops in cluster halos. Fitting dynamical models depends crucially on the availability of kinematic data, since surface brightness or star count profiles alone do not strongly constrain such important parameters as the mass function's slope or the total cluster mass.

In addition to evolving as a result of internal energy transport, clusters also respond to external tidal perturbations from interactions with the Galaxy. Such perturbations include shocks caused by the cluster's passage by the bulge or through the disk and a steady tidal acceleration from the smoother halo potential. In both cases, there is energy input to the cluster, producing a "heating" effect, although the latter is usually treated as a boundary condition causing the clusters to lose mass. While the energy is primarily deposited directly in the outer part of the cluster's mass distribution, as was first demonstrated by Spitzer & Chevalier (1973), the evolution of the entire cluster is affected. In particular, tidal shocking tends to accelerate core collapse.

The extent of tidal heating and its effect on the evolution of a cluster has been of continuing theoretical interest. A particular motivation is that tidal heating appears to be a major contributing factor to the destruction of globular clusters (Aguilar, Hut, & Ostriker 1988; Okazaki & Tosa 1995; Capriotti & Hawley 1996; Gnedin & Ostriker 1997). Kundić & Ostriker (1995) have given the most recent theoretical analysis of the expected heating of globular clusters by tidal shocks. They have shown that the second-order tidal shock relaxation term, neglected in many previous studies, is usually more important than the first-order term, both for the impulse and adiabatic approximations. Weinberg (1994) demonstrated that the usual adiabatic approximation does not apply in a three-dimensional potential, and this has been included in the analysis of Kundić & Ostriker (1995). From their analysis, it appears that tidal effects are locally important as far into a cluster as the half-mass radius.

Of particular relevance for comparison with the observations of the global velocity dispersion profile of M15 presented here are models for cluster evolution that include tidal effects. What are needed are numerical predictions with which to compare our velocity distribution observations. Unfortunately, most papers dealing with this have failed to provide an analysis that may be directly compared with the usual velocity dispersion profile determinations. One exception is Allen & Richstone (1988). This study,

[1] Table 2 in this paper contains the velocities of the 230 stars deemed to be members of the cluster. A table of 361 nonmember stars with velocities will not be published; this table and Table 2 are both available electronically from the Astronomical Data Center (ADC). The ADC's Internet site hosts WWW and FTP access to the ADC's archives at the URL http://adc.gsfc.nasa.gov.

which looked only at the first-order effect, found that the velocity dispersion increases for the escaping stars found in the outermost part of a cluster. They determined the tidal radius by the minimum in the velocity dispersion profile. This tidal radius and the difference between the radial and tangential velocity dispersion profiles depended on the nature of the assumed cluster orbit. Oh & Lin (1992) present a hybrid approach, which uses a Fokker-Planck approach for treating internal relaxation (using the second-order Fokker-Planck terms only) and direct orbit integration for including the effects of the tidal field. However, they do not provide results for the evolution of the velocity dispersion profile.

1.2. *Observational Background*

As the prototypical collapsed-core globular cluster, M15 has received considerable observational attention. Recent *Hubble Space Telescope* (*HST*) imaging studies have probed the stellar distribution in the central region with increasingly higher angular resolution (Lauer et al. 1991; De Marchi & Paresce 1994, 1995; Guhathakurta et al. 1996; Sosin & King 1997). The current consensus of this work is that the surface density profile of M15 has a central power-law form, with no clear evidence for a resolved core. The tightest upper limit on the core radius is 1".5 (Sosin & King 1997). These results have been combined with ground-based surface brightness measurements (Lugger, Cohn, & Grindlay 1995) and star counts (King et al. 1968) to generate a global surface density profile for Fokker-Planck model fits (Dull et al. 1997). The structure of the outermost region of M15 has recently been studied by Grillmair et al. (1995). They carried out two-color stellar photometry using digitized Schmidt plates and used the color-magnitude diagram to statistically correct for foreground contamination, thus allowing them to map out the large-radius density profile of the cluster. They found an apparent tidal radius of 23′ for M15, based on a King (1966) model fit. They also found an excess population of cluster stars beyond this radius, which they interpreted as a tidal tail.

A number of studies have been carried out over the past decade to determine the velocity dispersion profile of M15 (Peterson, Seitzer, & Cudworth 1989; Gebhardt et al. 1994, 1997; Dull et al. 1997). These studies have all concentrated on the central region of the cluster. The greatest radial offset for any star in the Peterson et al. (1989) sample is 4′.6; the other studies surveyed the central 1′–2′ radius about the cluster center. Peterson et al. (1989) and Dull et al. (1997) used long-slit spectroscopy, while Gebhardt et al. (1994, 1997) used Fabry-Perot imaging spectrophotometry to scan the Hα line.

The key finding by Peterson et al. (1989) is that the velocity dispersion profile of M15 rises rapidly toward the cluster center. While subsequent studies by Gebhardt et al. (1994, 1997) and Dull et al. (1997) confirm the rising nature of the profile within the central arcminute, these recent studies, plus that Dubath, Meylan, & Mayor (1994), obtained central velocity dispersions between 11 and 14 km s^{-1}, much less than the 25 km s^{-1} found by Peterson et al. (1989). As discussed by Dull et al. (1997), the global surface density profile of M15 and the velocity dispersion profile out to about 4′ are well fitted by a Fokker-Planck model that contains a substantial, centrally concentrated population of nonluminous remnants, presumably neutron stars. Multimass King-type models do not provide as good a joint fit to the surface density and velocity dispersion profiles (Dull et al. 1997; Sosin & King 1997).

In this study, we present the first velocity information for the outermost region of M15. The 230 cluster members identified in our sample lie primarily in the range 1′ − 16′.6 from the cluster center. Thus, our work complements that of Gebhardt et al. (1997), who have presented velocities for 1534 stars that primarily lie within 1′.5 of the cluster center. Our median velocity accuracy is 0.3 km s^{-1}; the velocity accuracies for the Gebhardt et al. (1997) sample vary over a range of 0.5–10 km s^{-1}.

In § 2, we describe our observations and present our velocity measurements. Our analysis technique, which is new for this application, uses Bayesian statistical methods. These are described in § 3; § 4 gives our analysis of the velocities of the members. In § 5, we interpret our results in the context of models for clusters evolving under the influence of tidal effects.

2. DATA

2.1. *Observations*

All of the new observations discussed here were obtained using the Hydra multifiber spectrograph on the 3.5 m WIYN telescope.[2] This instrument has 100 fibers that can each be placed within the 1° diameter observing field to 0".2 precision. The minimum fiber separation is 36", so while the central 0′.5 of the cluster cannot be efficiently observed, this instrument is ideal for observing the outer regions of globular clusters. We were able to observe up to 80 stars at a time. For all observations we used the echelle grating with an order centered at 515 nm, in the neighborhood of the Mg *b* lines. Approximately 20 nm of the order was imaged on the 2048 pixel–long CCD, for a dispersion of about 0.01 nm $pixel^{-1}$. The comparison source was a ThAr lamp.

Use of the Hydra spectrograph requires accurate positions for the stars to be observed. The positions of the stars came from two sources, a 3 × 3 mosaic of Curtis-Schmidt frames in V and I and a list from K. Cudworth of the stars on his M15 proper-motion program. This list filled in the center of the cluster, which was too crowded on the Schmidt frames to allow accurate photometry. The positions of the stars were reduced to the astrometric system of the *HST* Guide Star Catalog and proved, at the telescope, to be very reliable.

The input list contained over 13,000 stars, the bulk of which are nonmembers. Given our choice of spectral region, we restricted our observations to stars on the giant branch. Our candidates were therefore selected to lie in this region of the V versus $V-I$ color-magnitude diagram. We observed M15 during the course of three observing runs, one each in 1996 May, June, and October. Table 1 contains a log of the observations. The 1996 May run was in a sense experimental and took place before the full input list was produced. We only had astrometry from the central Schmidt frame, as well as the positions of K. Cudworth's stars. Because of the restricted region of candidates, we could only observe ∼25 stars per Hydra setup. In 1996 June the full list was available, and we observed virtually all the stars on the giant branch brighter than $V = 15.7$ and

[2] The WIYN Observatory is a joint facility of the University of Wisconsin, Indiana University, Yale University, and the National Optical Astronomy Observatories.

TABLE 1

OBSERVATION LOG

Setup ID	UT Date (1996)	Total Exposure (s)
Central 1......	May 15	2400
Central 2......	May 15	1800
K1............	May 17	4800
K2............	May 19	3000
A	Jun 19	2100[a]
B..............	Jun 19	2100[a]
C	Jun 22	1800
D	Jun 22	1800
E..............	Jun 23	1800
F..............	Jun 23	1800
H	Oct 11	4500
N	Oct 11	4800
I	Oct 12	7200
O	Oct 12	6000
P..............	Oct 13	11500[a]
Q	Oct 14	4811[a,b]
Q	Oct 15	6000[b]
R	Oct 15	9300

[a] Observations affected by clouds.

[b] Spectra from both nights combined. Total exposure time is 10811 s.

outside about 4′. In 1996 October we reobserved all the known members between 4′and 18′, some of the central stars, and an additional sample on the giant branch with $15.7 < V < 16.6$ and $4' < r < 17'$. As the October run progressed, we performed rough reductions of the spectra to weed out nonmembers and to obtain additional spectra of apparent members. Figure 1 displays the distribution of observed stars in radius and magnitude. The diagram is a version of a "sunflower" plot (Cleveland & McGill 1984). The number of points on each symbol represents the number of observations, stars observed once (*circles*) and twice (*diagonal lines*). We obtained, in total, 1132 spectra of 591 stars in the M15 field. Of these, 230 turned out to be members. Membership was determined by velocity coherence and the strength of the absorption lines, and will be discussed further below.

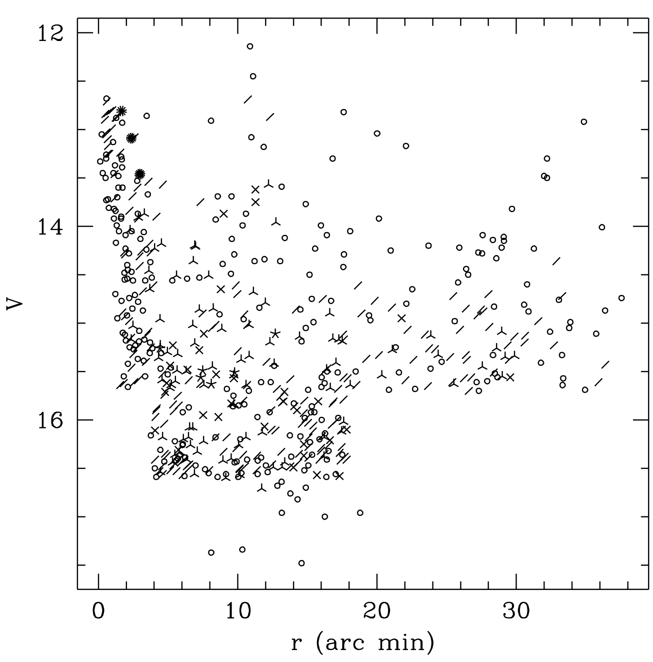

FIG. 1.—Distribution of observed stars in radial position and V magnitude. The number of points on each symbol represents the number of observations. A small circle represents a single observation and a diagonal line represents two observations.

At least one of the stars K144 and K1040 was observed in each Hydra configuration ("setup"). The former proved to have a variable radial velocity which changed by 1 km s^{-1} between May and June and 1.4 km s^{-1} between June and October. The velocities for K1040 were much more consistent, and its spectrum was used as the template for the velocity determination by cross-correlation.

2.2. *Spectral Reduction*

The data were reduced using the DOHYDRA reduction package in IRAF.[3] Each observation was accompanied by one or more 5 minute exposures of an incandescent lamp (a "flat") taken with the fibers in the same configuration as the observations. Generally, setups observed at the ends of the night had multiple-flat exposures, but, because of the overhead involved with flats and especially with reconfiguring the fibers, usually single-flat exposures were done. There did not appear to be any disadvantage to using single exposures, since cosmic rays were not a great problem. The program exposures and bracketing ThAr lamp exposures were extracted and then divided by the extracted lamps. No sky subtraction was required, because of the high dispersion and the absence of the Moon; all observations were taken in dark time. The wavelength calibration was accomplished using 36 comparison lines. The fifth-order dispersion solution generally had rms residuals of less than 10^{-4} nm, or 0.05 km s^{-1}. During dispersion correction, the spectra were resampled into 2048 logarithmically spaced bins covering 20.7 nm in total.

Cosmic-ray removal was accomplished through the simple expedient of using the IRAF CONTINUUM task to replace with the continuum fit all pixels more than 4 σ above the fit or 9 σ below the fit. The latter was necessary because of the resampling of the spectra during dispersion correction. The spline interpolation required for resampling sometimes gave complementary negative spikes around large cosmic rays. Care was taken not to remove any genuine absorption lines. Some artificial lines, arising in resampling but falling under the 9 σ limit, may have been added, but this would not have had a large effect on the resulting velocities, given the large number of real lines dominating the cross-correlation.

In 1996 May and October, multiple exposures were taken with each fiber configuration. The resulting spectra were added together to produce the final spectra for cross-correlation. The four exposures in the October "Q" configuration were taken on two consecutive nights because of clouds, but were nevertheless combined, since the faintest stars lacked adequate flux in either pair. These were first shifted by a velocity equivalent to the difference in Earth's heliocentric velocity relative to M15 between the two observations.

[3] IRAF is distributed by the National Optical Astronomy Observatories, which are operated by the Association of Universities for Research in Astronomy, Inc., under cooperative agreement with the National Science Foundation.

2.3. *Cross-Correlation, Velocity Uncertainties, and the Zero Point*

There were 33 individual exposures of K1040, totaling over 22 hr of exposure time. These were shifted to remove small differences in the geocentric velocity and were summed to form the high signal-to-noise ratio template shown in Figure 2. The stellar velocities were measured relative to this template using the cross-correlation technique of Tonry & Davis (1979) encoded in the IRAF FXCOR task. This computes the cross-correlation function of the Fourier transforms of the template and stellar spectra. The shift of the cross-correlation peak from zero gives the velocity of the program star relative to the template. This was computed for all the extracted stellar spectra. We excluded from further analysis all spectra with cross-correlation peaks less than 0.2. These spectra had low signal-to-noise ratios, and the velocities derived were often obviously due to the selection of chance peaks in the cross-correlations, since they often yielded velocities of several thousand km s^{-1}.

The uncertainties in the velocities, ϵ_v, were determined from the ratio, R, of the peak of the cross-correlation function to the size of the random-noise fluctuations. For each spectrum $\epsilon_v = C/1 + R$ (Tonry & Davis 1979). The constant C depends on the number of resolution elements in the observation and on the width of the cross-correlation function. In practice, the value of C is established from the data. We have used the procedure of Pryor, Latham, & Hazen (1988) to calculate C. For all stars observed more than once in an observing run, we have computed the statistic

$$\epsilon = \frac{\Delta v}{[(1 + R_1)^{-2} + (1 + R_2)^{-2}]^{1/2}} . \quad (1)$$

After weeding out possible variables, we have 228 pairs of repeat observations. Using the Bayesian procedure described in § 3, we have calculated the dispersion of the distribution of ϵ assuming a zero mean. This yields $C = 13.1 \pm 0.5$ km s^{-1}, which is the value used in computing the errors in the velocity tables.

The velocity zero point was established using six high signal-to-noise ratio exposures of the twilight sky, two taken in 1996 May and four in 1996 October. The fibers in these exposures had various configurations. The spectra in these exposures were extracted and wavelength-calibrated in the usual way, and these individual spectra were cross-correlated against the K1040 template spectrum. The average velocity for the spectra in each sky exposure was calculated. The internal dispersions were between 0.10 and 0.24 km s^{-1}, and the mean error in a single velocity was 0.6 km s^{-1} using $C = 13.1$ km s^{-1} as above. The difference between the internal dispersion and the individual uncertainties might suggest that the individual errors are overestimated. On the other hand, the standard deviation of the six mean velocities about their mean is 0.5 km s^{-1}, which is quite consistent with the error estimate. What this indicates is that while the velocities of the spectra in an exposure can be measured consistently, there are systematic differences between exposures as well. Since there is agreement between the standard deviation of the velocities in the six exposures and the errors of the individual velocities, we can have some confidence that our value for C, and hence for the uncertainties, is correct. This is important for the subsequent calculation of the cluster velocity dispersion. The zero point is taken as the unweighted mean of the six mean velocities and is -99.4 ± 0.2 km s^{-1}. The velocity of K1040 itself is derived in the same way as for the rest of the stars. Its mean velocity with respect to the template is 0.04 ± 0.03 km s^{-1}.

As a final check we compare our velocities against the velocities of stars in common with those observed by Peterson et al. (1989) and Gebhardt et al. (1997). Figures 3 and 4 compare the velocities of the common stars. There are 79 stars in common between our data and Peterson et al. (1989) and 42 between our data and Gebhardt et al. (1997); we have only included the new velocities reported by Gebhardt et al. The outlying star in Figure 3 is K673, which is claimed by Gebhardt et al. (1994) to be a binary. The Peterson et al. velocity is the most discrepant. Most of the stars in Figure 4 lying off of the equality line are noted as being variable in one of these studies. For four of the Gebhardt et al. variables, we also have multiple observations, and we confirm three of them. One further possible variable is not confirmed. The apparent zero-point shift is not statistically significant for the full sample, but for the nonvariables, there is a correlation between declination and velocity dif-

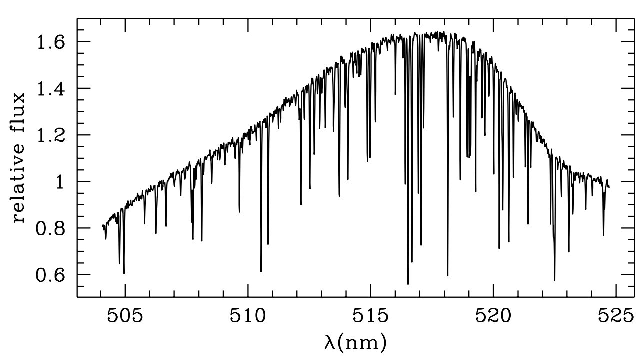

FIG. 2.—Template spectrum used for cross-correlations. This is a combination of 33 individual spectra of K1040 adjusted for heliocentric velocity differences.

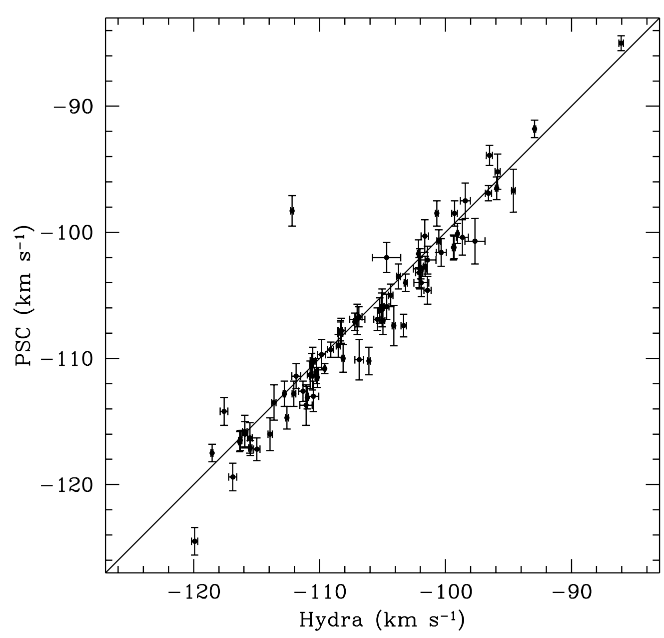

FIG. 3.—Comparison of our velocities with those of Peterson et al. (1989). The star with a large deviation is K673, a probable variable.

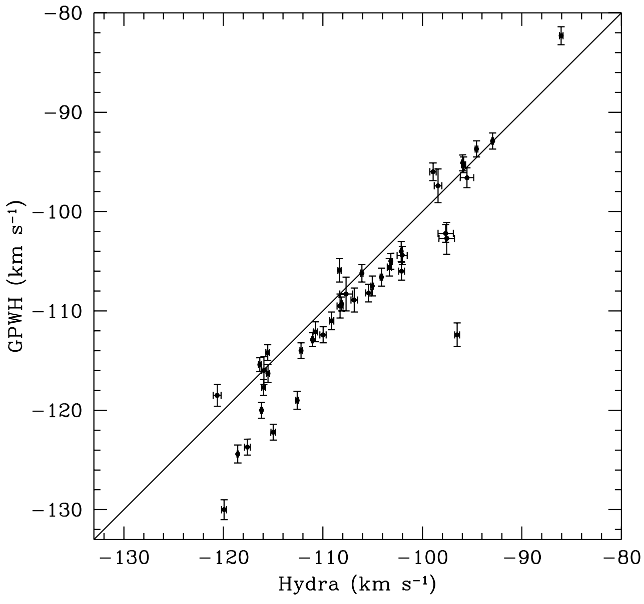

FIG. 4.—Comparison of our velocities with the Fabry-Perot velocities of Gebhardt et al. (1994, 1997).

ference amounting to 5 km s^{-1} across the Fabry-Perot field. Taking this into account, there appears to be a zero-point difference of 0.9 km s^{-1} between the two data sets. These differences may indicate a systematic problem with the Fabry-Perot calibration.

Calculation of the mean velocity differences for the full samples of the two comparisons yields dispersions about the means that are somewhat larger than expected if the adopted errors in each study are correct. Gebhardt et al. (1997) note that their measurement uncertainties are still not fully understood but the Peterson et al. (1989) uncertainties apparently are. Thus, in Figure 5 we show, against V magnitude, χ^2 for the two observations with respect to their mean for the comparison with Peterson et al. (1989) sample. There is a difference in behavior for stars on either side of $V = 13.3$. There appears to be extra variance for the stars brighter than $V = 13.3$. This is probably due to the velocity "jitter" observed for stars near the tip of the giant branch in many clusters (Gunn & Griffin 1979; Mayor et al. 1984; Lupton, Gunn, & Griffin 1987; Pryor et al. 1988). Peterson et al. (1989) attribute the excess variance in their repeat observations to an internal jitter of 0.88 km s^{-1}. The observations by Gebhardt et al. (1997) are generally not precise enough to see this effect. If we restrict our comparison to stars with $V > 13.3$, then the difference distribution is consistent with unit variance. This gives us confidence that our uncertainties have been calculated correctly. The question of the "jitter" will be addressed further in the next section.

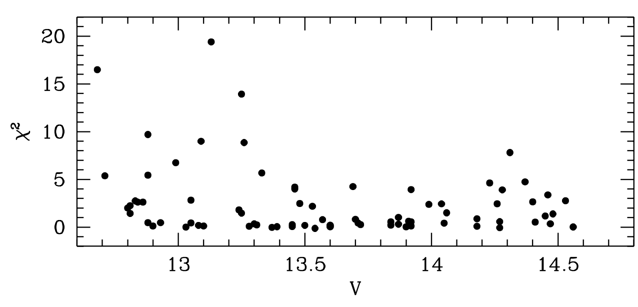

FIG. 5.—For the stars in common with Peterson et al. (1989) we show χ^2 vs. magnitude. Note the extra variance apparent for stars brighter than $V = 13.3$. This can be attributed to the jitter seen in the velocities of bright giants.

2.4. *Velocities*

In total we have measured 1132 velocities for 591 stars in the field of M15. Figure 6 shows the measured velocities plotted against distance from the cluster center. This was taken to be $\alpha = 21^h29^m58\overset{s}{.}6$, $\delta = +12°10'1\overset{''}{.}0$ (J2000.0) (Guhathakurta et al. 1996). Generally, the cluster members stand out quite distinctly from the nonmembers based on the velocity difference of approximately 100 km s^{-1} between the cluster and the foreground disk stars. We selected the cluster members by first excluding all stars with velocities greater than 40 km s^{-1} with respect to K1040. The spectra of all the rest of the stars were examined individually to estimate the equivalent widths of the Mg *b* lines. These lines are a sensitive luminosity indicator, but less so as a metallicity indicator (Geisler 1981), allowing us to distinguish between cluster giants and field dwarfs. All the stars with large equivalent widths were rejected as being field Population I dwarf stars. A few of the stars in the field region, those with the lowest velocities with respect to K1040, were also examined to check for high-velocity cluster members as have been seen in 47 Tuc (Meylan, Dubath, Mayor 1991). None were found. We also examined the spectra of nine stars with velocities greater than 40 km s^{-1} with respect to K1040 that K. Cudworth (1996, private communication) had assigned membership probabilities in excess of 50% based on their proper motions. All of these had high Mg *b* equivalent widths. There was also a population of a dozen stars with velocities significantly more negative than that of the cluster. Several of these had very weak spectra, which precluded estimates of the equivalent widths. Their velocities may be suspect. Most of the others had equivalent widths larger than the typical

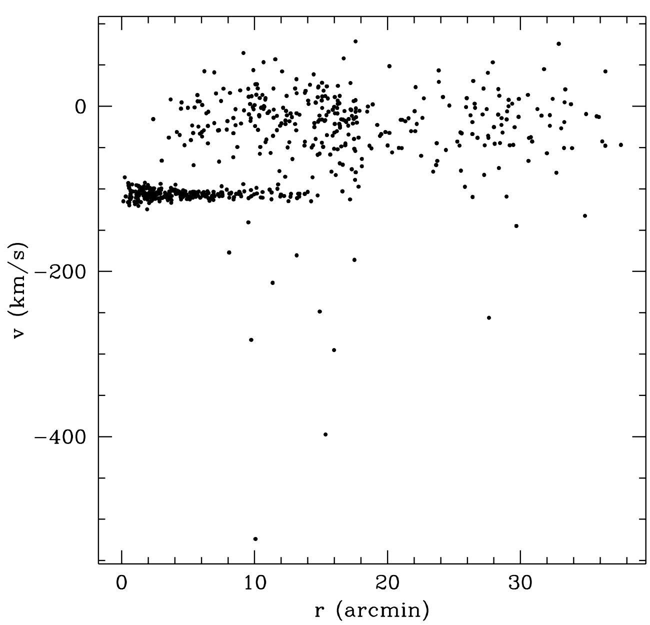

FIG. 6.—Velocities for all the stars observed in this study plotted against their radial positions. The cluster stands out as the clump with velocity near -107 km s^{-1}. The stars around zero velocity are disk stars, while the stars with very negative velocities probably belong to the halo.

TABLE 2

MEAN VELOCITES OF MEMBER STARS

R.A. (J2000.0) (1)	Decl. (J2000.0) (2)	ID (3)	V (4)	No. (5)	v (6)	ϵ_v (7)	$P(\chi^2)$ (8)	Other Name (9)	Notes (10)
21 29 05.12	+11 59 40.7	9494	14.90	3	−102.91	0.21	0.326		
21 29 08.40	+12 09 12.6	B5	13.57	3	−108.53	0.11	0.004		j
21 29 10.70	+12 16 37.7	9300	16.44	3	−105.78	0.35	0.249		
21 29 12.32	+12 10 50.6	B6	13.62	4	−112.56	0.07	0.034		
21 29 13.02	+12 11 15.7	C3	14.68	3	−100.86	0.14	0.058		
21 29 17.36	+12 16 37.2	C8	14.79	3	−106.82	0.15	0.272		
21 29 20.04	+12 14 00.6	8940	16.57	3	−105.49	0.54	0.153		
21 29 20.93	+12 13 22.0	8907	15.57	4	−101.43	0.35	0.995		
21 29 30.66	+12 10 38.0	8541	16.08	3	−109.17	0.38	0.697		
21 29 30.74	+12 06 33.3	K12	15.11	4	−106.59	0.23	0.811		
21 29 33.10	+12 12 51.6	K21	15.02	3	−111.60	0.31	0.887		
21 29 33.50	+12 04 56.0	K22	14.51	3	−100.88	0.13	0.649		
21 29 34.07	+11 59 39.4	8335	16.07	4	−109.21	0.24	0.124		
21 29 34.60	+12 03 20.0	K26	15.06	3	−103.53	0.19	0.701		
21 29 35.05	+12 06 04.3	K27	15.21	3	−106.45	0.29	0.032		
21 29 35.28	+12 14 08.9	K29	14.21	3	−108.96	0.13	0.740		
21 29 35.84	+12 08 28.1	K31	15.32	3	−105.15	0.21	0.250		
21 29 36.45	+12 03 55.4	K34	15.63	5	−105.75	0.30	0.497		
21 29 37.10	+12 13 41.3	8195	16.48	2	−107.12	0.92	0.753		
21 29 37.15	+12 08 09.8	8184	16.36	3	−105.33	0.44	0.753		
21 29 37.97	+12 11 58.9	K42	15.23	4	−103.61	0.26	0.100		
21 29 39.34	+12 12 39.4	8062	16.44	3	−105.95	0.48	0.111		
21 29 39.39	+12 18 21.6	8063	15.83	4	−111.22	0.18	0.244		
21 29 40.02	+12 16 00.7	K56	15.49	5	−104.20	0.21	0.902		
21 29 40.12	+12 05 19.6	8005	16.18	3	−102.87	0.62	0.530		
21 29 40.16	+12 08 24.0	8007	16.04	2	−103.32	0.44	0.722		
21 29 41.24	+12 07 20.1	K60	15.30	3	−109.08	0.29	0.525		
21 29 41.70	+12 03 37.8	K62	15.64	3	−108.53	0.38	0.683		
21 29 42.54	+12 07 28.0	7873	16.56	2	−101.71	0.61	0.411		
21 29 42.93	+12 09 54.2	K64	15.25	2	−108.65	0.43	0.253		
21 29 43.49	+12 10 04.1	K66	14.46	3	−104.96	0.14	0.781		
21 29 43.56	+12 15 48.0	K703	14.36	3	−108.25	0.14	0.619		
21 29 43.76	+12 06 16.2	7783	16.52	2	−104.31	0.45	0.622		
21 29 43.76	+12 08 34.0	K69	14.53	1	−101.92	0.56	...		
21 29 44.62	+12 07 31.4	K77	13.90	2	−103.74	0.15	0.335		
21 29 44.66	+12 05 08.4	7725	16.44	2	−110.59	0.65	0.338		
21 29 44.94	+12 06 31.0	K81	15.71	4	−102.90	0.40	0.833		
21 29 45.78	+12 08 46.2	K87	13.87	3	−108.52	0.16	0.290		
21 29 46.03	+12 11 32.2	K89	14.56	1	−109.84	0.32	...		
21 29 46.67	+12 03 21.4	K92	15.28	4	−106.23	0.23	0.008		v
21 29 46.74	+12 16 18.4	7586	16.56	3	−113.48	0.51	0.666		
21 29 46.84	+12 11 45.7	K97	15.17	1	−107.47	0.67	...		
21 29 46.86	+12 12 58.3	7573	16.11	4	−106.08	0.33	0.142		
21 29 46.91	+12 08 27.3	K95	14.87	1	−109.62	0.97	...		
21 29 47.35	+12 09 05.3	K105	15.37	1	−112.63	0.76	...		
21 29 47.82	+12 06 44.8	7490	15.90	2	−105.80	0.34	0.588		
21 29 47.83	+12 08 46.1	K114	13.92	2	−112.81	0.11	0.000		v
21 29 47.91	+12 05 48.9	7483	16.37	2	−112.38	0.48	0.087		
21 29 48.50	+12 20 20.5	7463	16.18	3	−110.71	0.27	0.659		
21 29 48.53	+12 06 44.6	7440	16.50	1	−94.92	1.19	...		
21 29 48.59	+12 11 46.4	K129	14.31	2	−101.43	0.29	0.818		
21 29 48.69	+12 06 39.1	7427	15.97	2	−105.16	0.40	0.152		
21 29 48.81	+12 10 25.9	K133	15.17	3	−104.48	0.39	0.072		
21 29 49.09	+12 09 04.4	K136	14.85	1	−109.16	0.50	...		
21 29 49.67	+12 09 24.1	K141	14.98	2	−103.25	0.39	0.802		
21 29 49.75	+12 11 06.6	K144	13.09	16	−109.59	0.04	0.000		j
21 29 49.76	+12 12 30.6	K145	15.39	1	−109.35	0.56	...		
21 29 49.89	+12 18 12.9	K153	15.53	4	−110.09	0.24	0.443		
21 29 49.91	+12 08 05.9	K146	13.60	2	−100.53	0.14	0.493		
21 29 49.91	+12 14 07.6	K150	15.53	2	−109.83	0.37	0.771		
21 29 50.07	+12 15 43.1	7328	16.57	2	−105.44	0.55	0.303		
21 29 50.10	+12 07 52.9	K151	15.08	1	−93.86	0.53	...		
21 29 50.12	+12 09 34.0	K154	14.92	1	−109.44	0.37	...		
21 29 50.14	+12 06 41.4	K152	15.26	1	−100.68	0.67	...		
21 29 50.24	+12 09 03.6	K158	14.28	1	−110.49	0.40	...		
21 29 50.48	+12 20 18.9	C18	14.91	2	−110.36	0.31	0.755		
21 29 51.30	+12 09 39.2	K181	15.10	1	−92.47	0.96	...		
21 29 51.39	+11 56 50.7	7186	15.81	4	−105.83	0.21	0.796		
21 29 51.43	+12 08 11.2	K185	14.56	1	−107.01	0.58	...		
21 29 51.51	+12 11 58.4	7204	15.61	2	−111.49	0.39	0.690		
21 29 51.61	+12 12 05.0	K197	15.23	1	−104.18	0.72	...		

TABLE 2—*Continued*

R.A. (J2000.0) (1)	Decl. (J2000.0) (2)	ID (3)	V (4)	No. (5)	v (6)	ϵ_v (7)	$P(\chi^2)$ (8)	Other Name (9)	Notes (10)
21 29 51.67	+12 08 30.8	7179	14.74	1	−114.85	1.07	…		
21 29 51.81	+12 14 28.9	7174	15.74	2	−108.32	0.32	0.529		
21 29 51.82	+12 08 56.1	K205	14.93	2	−110.60	0.27	0.489		
21 29 51.86	+12 06 39.5	K202	15.20	1	−98.78	0.57	…		
21 29 52.27	+12 19 40.4	C20	15.51	5	−108.66	0.23	0.361		
21 29 52.28	+12 10 52.1	K224	13.39	1	−106.88	0.84	…		
21 29 52.41	+12 06 59.2	7108	15.55	1	−110.25	0.93	…		
21 29 52.41	+12 07 59.3	K228	15.03	3	−110.57	0.32	0.193		
21 29 52.61	+12 10 44.6	K238	13.24	2	−101.61	0.15	0.129		
21 29 52.64	+12 04 40.6	7081	15.60	3	−108.70	0.28	0.024		
21 29 52.72	+12 11 02.4	K240	12.93	1	−104.35	0.82	…		
21 29 52.81	+12 14 16.7	7084	16.54	3	−112.50	0.43	0.224		
21 29 53.08	+12 12 31.8	K255	13.87	1	−101.64	0.28	…		
21 29 53.11	+12 11 03.2	K254	13.28	1	−108.34	0.82	…		
21 29 53.27	+12 04 21.2	7036	16.34	3	−103.13	0.50	0.398		
21 29 53.27	+12 09 34.7	K260	13.99	1	−97.66	0.77	…	Geb 1463	
21 29 53.54	+12 09 11.3	K272	13.48	1	−105.41	0.84	…	Geb 1526	
21 29 53.76	+12 10 21.0	K288	13.71	2	−105.04	0.13	0.043	Geb 1369	
21 29 53.80	+12 09 34.5	K290	13.37	1	−115.94	0.82	…	Geb 1397	
21 29 54.16	+12 10 55.6	K309	14.95	1	−97.55	0.78	…	Geb 1490	
21 29 54.67	+12 01 06.7	6921	16.42	3	−106.33	0.38	0.614		
21 29 54.69	+12 08 59.9	K328	13.70	1	−102.09	0.28	…	Geb 1484	
21 29 54.90	+12 13 23.2	K341	12.86	1	−110.19	0.81	…		
21 29 54.96	+12 11 45.4	6914	14.29	2	−124.79	0.39	0.162		
21 29 55.01	+12 02 49.2	K337	14.86	3	−106.93	0.26	0.069		
21 29 55.25	+12 16 08.6	6894	16.41	2	−103.81	0.42	0.042		
21 29 55.32	+12 15 05.9	6883	15.67	3	−112.49	0.36	0.048		
21 29 55.43	+12 11 04.9	K373	12.88	1	−96.51	0.84	…	Geb 1443	
21 29 55.56	+12 09 07.4	K383	13.82	1	−95.51	0.68	…	Geb 1347	
21 29 55.57	+12 12 42.9	K387	13.53	1	−111.31	0.87	…		
21 29 55.59	+12 10 46.2	K386	12.80	2	−118.54	0.08	0.063	Geb 1266	
21 29 55.61	+12 11 43.1	6852	15.62	2	−106.72	0.35	0.479		
21 29 55.69	+12 11 34.5	K393	13.31	1	−96.59	0.84	…		
21 29 55.72	+12 07 59.7	6838	15.66	1	−99.92	0.70	…		
21 29 55.87	+12 09 33.2	K406	13.81	1	−109.98	0.31	…	Geb 1048	
21 29 56.14	+12 10 18.4	K421	12.71	2	−111.04	0.09	0.000	Geb 847	j
21 29 56.15	+12 12 34.5	K431	13.08	2	−107.20	0.12	0.016		
21 29 56.26	+12 09 55.0	K435	13.50	1	−95.86	0.82	…	AC 529	
21 29 56.35	+12 14 45.9	6791	16.35	2	−106.27	0.67	0.611		
21 29 56.41	+12 10 30.0	K447	13.25	2	−106.08	0.11	0.882	Geb 945	
21 29 56.53	+12 11 56.8	K460	15.18	1	−95.42	0.58	…		
21 29 56.63	+12 09 47.0	K462	12.90	2	−116.16	0.11	0.000	AC 13	j
21 29 56.67	+12 14 36.3	6763	16.18	3	−105.35	0.76	0.095		
21 29 56.69	+12 13 11.3	K476	14.67	2	−108.90	0.26	0.026		
21 29 56.76	+12 10 27.5	K479	12.68	1	−119.92	0.84	…	Geb 824	
21 29 56.99	+12 09 38.2	K490	12.84	2	−92.94	0.08	0.000	AC 463	j
21 29 57.02	+12 08 53.7	K488	13.46	2	−104.11	0.12	0.775	Geb 1376	
21 29 57.11	+12 04 22.8	K486	15.49	3	−106.89	0.28	0.931		
21 29 57.36	+12 10 38.5	K511	13.10	2	−102.12	0.09	0.000	AC 808	j
21 29 57.40	+12 08 22.1	K506	14.77	1	−103.30	0.49	…		
21 29 57.76	+12 09 28.6	K531	13.05	2	−95.95	0.11	0.011	Geb 792	
21 29 57.98	+12 14 26.9	K553	14.96	3	−109.76	0.24	0.584		
21 29 58.00	+12 11 54.9	K550	15.12	1	−109.59	0.58	…		
21 29 58.25	+12 08 10.1	K560	14.27	2	−99.28	0.22	0.749		
21 29 58.27	+12 04 33.7	6607	16.41	2	−103.49	0.54	0.000		v
21 29 58.29	+12 09 13.4	K567	13.25	2	−94.57	0.14	0.000	Geb 1087	j
21 29 58.31	+12 09 46.6	K570	13.05	b	−86.05	0.82	…	AC 411	
21 29 58.35	+12 10 42.2	K578	13.72	1	−102.03	0.50	…	Geb 968	
21 29 58.53	+12 09 22.0	K583	12.83	2	−108.12	0.09	0.000	Geb 924	1
21 29 58.56	+12 08 08.6	K582	14.48	1	−98.66	0.46	…		
21 29 58.68	+12 08 56.7	K589	13.45	1	−110.75	0.83	…	Geb 1315	
21 29 58.70	+12 08 32.9	K592	14.05	1	−98.43	0.38	…	Geb 1539	
21 29 58.77	+12 09 56.8	AC 111	13.33	1	−114.98	0.84	…		
21 29 58.81	+12 10 17.9	AC 761	13.45	1	−109.12	0.83	…		
21 29 59.28	+12 09 12.3	K634	12.81	2	−103.16	0.12	0.334	Geb 1141	
21 29 59.42	+12 08 36.1	K647	13.60	1	−115.93	0.22	…	Geb 1529	
21 29 59.75	+12 11 00.5	K670	13.13	1	−103.32	0.83	…	Geb 1295	
21 29 59.78	+12 11 11.4	K672	13.84	1	−108.28	0.30	…	Geb 1420	
21 29 59.80	+12 09 26.4	K673	13.17	2	−112.18	0.11	0.006	Geb 972	j
21 29 59.85	+12 12 29.6	K682	15.32	2	−112.15	0.40	0.944		
21 29 59.95	+12 06 27.3	K677	15.09	2	−103.25	0.36	1.000		
21 30 00.00	+12 13 40.4	K691	14.65	3	−109.31	0.23	0.453		

TABLE 2—*Continued*

R.A. (J2000.0) (1)	Decl. (J2000.0) (2)	ID (3)	V (4)	No. (5)	v (6)	ϵ_v (7)	$P(\chi^2)$ (8)	Other Name (9)	Notes (10)
21 30 00.24	+12 09 41.6	K706	13.03	2	−116.33	0.14	0.000	Geb 809	b
21 30 00.24	+12 14 25.7	K714	15.23	3	−105.09	0.44	0.583		
21 30 00.30	+12 10 51.4	K702	12.99	2	−115.51	0.15	0.065	Geb 1241	
21 30 00.34	+12 07 37.1	K709	13.69	2	−99.33	0.13	0.493		
21 30 00.54	+12 10 04.8	K733	13.30	1	−115.54	0.82	...	AC 11	
21 30 00.58	+12 10 02.1	K734	13.26	1	−117.59	0.85	...	AC 650	
21 30 00.59	+12 10 06.4	K735	13.73	1	−98.93	0.31	...	AC 651	
21 30 00.63	+12 22 33.2	6442	16.49	3	−114.86	0.40	0.094		
21 30 00.87	+12 08 57.8	K757	12.88	2	−112.59	0.12	0.110	Geb 1423	
21 30 01.08	+12 07 15.8	K769	15.59	2	−103.38	0.80	0.003		v
21 30 01.11	+12 12 18.0	K776	15.46	2	−99.58	0.39	0.693		
21 30 01.60	+12 12 30.8	K800	14.71	1	−104.52	0.44	...		
21 30 02.22	+12 11 22.4	K825	12.81	12	−99.03	0.05	0.000		b
21 30 02.60	+11 56 51.3	6246	16.49	3	−111.11	0.47	0.801		
21 30 02.70	+12 10 44.5	K853	12.88	2	−108.33	0.17	0.860	Geb 1454	
21 30 02.73	+12 06 56.6	K846	14.06	1	−104.68	0.20	...		
21 30 02.75	+12 11 28.5	6256	15.55	1	−105.60	0.66	...		
21 30 02.86	+12 10 08.9	K863	13.92	1	−106.85	0.33	...	Geb 1340	
21 30 03.06	+12 10 22.4	K866	14.70	1	−107.66	0.63	...	Geb 1415	
21 30 03.14	+12 13 29.5	K875	14.18	2	−110.55	0.20	0.964		
21 30 03.45	+12 10 04.7	K884	14.17	1	−120.62	0.40	...	Geb 1439	
21 30 03.47	+12 03 13.1	K879	14.20	3	−103.52	0.21	0.203		
21 30 03.97	+12 08 58.5	K902	14.89	2	−107.61	0.23	0.127		
21 30 04.07	+12 07 27.7	K906	15.19	1	−105.57	0.46	...		
21 30 04.18	+12 08 28.3	K912	14.45	1	−100.34	0.38	...		
21 30 04.28	+12 10 56.8	K919	13.60	1	−111.86	0.34	...		
21 30 04.58	+12 08 54.4	K925	14.55	1	−108.67	0.66	...		
21 30 04.59	+12 10 33.4	K928	13.92	1	−105.06	0.17	...		
21 30 04.62	+12 07 41.2	K926	15.25	2	−105.89	0.57	0.110		
21 30 04.71	+12 09 32.4	6080	13.90	1	−104.21	0.22	...		
21 30 04.71	+12 11 10.9	K932	14.09	1	−107.16	0.29	...		
21 30 04.77	+12 11 47.6	K934	14.47	1	−101.43	0.65	...		
21 30 04.81	+12 11 07.6	K936	14.23	1	−112.87	0.29	...		
21 30 05.15	+12 13 21.0	K947	14.37	1	−116.89	0.30	...		
21 30 05.50	+12 08 56.0	K954	14.40	1	−104.68	1.08	...		
21 30 05.51	+12 11 05.8	K956	14.54	1	−117.23	0.40	...		
21 30 05.54	+12 07 06.0	K953	15.40	2	−110.33	0.39	0.207		
21 30 05.82	+12 01 13.1	K957	13.87	4	−109.04	0.10	0.535		
21 30 06.23	+11 56 47.8	5934	15.71	4	−109.39	0.30	0.877		
21 30 06.33	+12 07 00.0	K969	13.54	2	−110.64	0.13	0.402		
21 30 06.57	+12 09 22.9	K973	15.42	1	−98.92	0.36	...		
21 30 06.93	+12 07 47.3	K979	14.26	2	−111.08	0.50	0.752		
21 30 06.95	+12 09 17.2	K981	15.25	1	−106.40	0.91	...		
21 30 07.26	+12 10 51.5	K989	15.15	2	−109.87	0.34	0.417		
21 30 07.31	+12 09 38.5	K990	13.84	2	-110.25	0.16	0.867		
21 30 07.36	+12 10 33.7	K993	14.04	3	−113.93	0.16	0.339		
21 30 07.46	+12 08 14.3	K994	13.91	3	−112.04	0.15	0.539		
21 30 07.99	+12 12 55.1	K1006	14.27	2	−113.61	0.17	0.332		
21 30 08.23	+12 04 08.9	5778	16.41	3	−107.46	0.50	0.718		
21 30 08.91	+12 08 49.9	K1014	14.78	1	−114.94	0.36	...		
21 30 09.52	+12 04 57.9	5668	16.31	4	−108.27	0.41	0.193		
21 30 09.68	+12 13 43.2	K1029	13.57	2	−101.97	0.18	0.542		
21 30 09.76	+12 12 55.1	K1030	14.23	3	−100.69	0.12	0.115		
21 30 09.86	+12 10 53.2	K1033	14.41	2	−110.57	0.22	0.213		
21 30 10.40	+12 11 49.6	5612	15.12	2	−113.53	0.54	0.391		
21 30 10.47	+12 10 07.0	K1040	13.46	17	−99.36	0.03	0.000		j
21 30 10.48	+12 15 54.8	5613	16.26	3	−114.50	0.42	0.306		
21 30 10.55	+12 14 12.1	K1042	15.44	4	−108.92	0.32	0.932		
21 30 11.20	+12 14 20.8	5555	15.84	2	−110.51	0.92	0.000		v
21 30 11.27	+12 01 49.3	K1049	14.65	4	−106.10	0.13	0.560		
21 30 11.35	+12 08 42.1	K1054	14.24	1	−106.63	0.41	...		
21 30 11.60	+12 14 06.5	5523	15.64	3	−107.97	0.30	0.484		
21 30 12.00	+12 04 23.7	5479	16.08	3	−105.03	0.62	0.773		
21 30 14.23	+12 09 24.4	K1069	14.61	2	−102.23	0.28	0.254		
21 30 14.68	+12 12 11.8	K1071	15.59	3	−108.17	0.27	0.272		
21 30 14.71	+12 08 25.0	K1070	15.36	3	−103.30	0.37	0.171		
21 30 15.19	+12 19 46.9	5304	15.64	3	−103.75	0.32	0.705		
21 30 15.20	+12 11 35.4	K1074	15.26	5	−106.96	0.16	0.063		
21 30 15.54	+12 05 12.0	K1076	15.48	4	−106.97	0.34	0.715		
21 30 15.62	+12 08 23.8	K1079	14.18	3	−105.22	0.13	0.562		
21 30 15.75	+12 17 00.4	K1083	15.45	3	−105.92	0.26	0.046		
21 30 16.04	+12 13 35.0	K1084	14.51	3	−104.17	0.14	0.725		

TABLE 2—*Continued*

R.A. (J2000.0) (1)	Decl. (J2000.0) (2)	ID (3)	V (4)	No. (5)	v (6)	ϵ_v (7)	$P(\chi^2)$ (8)	Other Name (9)	Notes (10)
21 30 16.65	+12 09 09.8	5205	16.48	2	−110.00	0.79	0.879		
21 30 17.30	+12 06 04.9	5168	16.20	3	−108.13	0.42	0.450		
21 30 18.11	+12 09 15.9	5138	15.62	4	−106.80	0.38	0.581		
21 30 20.34	+12 11 34.3	5044	16.53	2	−105.71	0.53	0.670		
21 30 21.00	+12 13 01.5	K1097	15.50	3	−109.15	0.26	0.654		
21 30 22.49	+12 14 23.2	K1104	15.56	5	−108.89	0.26	0.625		
21 30 22.68	+12 18 00.4	K1106	14.70	2	−106.45	0.34	0.944		
21 30 25.55	+12 17 06.0	4796	15.84	3	−109.32	0.30	0.458		
21 30 26.77	+12 07 04.8	4724	16.22	3	−104.27	0.50	0.676		
21 30 29.64	+12 20 11.8	B18	13.96	3	−105.98	0.17	0.878		
21 30 31.75	+12 08 55.7	K1136	14.85	3	−104.56	0.22	0.917		
21 30 32.48	+12 07 54.8	4483	15.97	4	−105.99	0.45	0.233		
21 30 44.10	+12 11 23.5	B30	13.75	4	−104.26	0.10	0.096		
21 30 49.26	+12 07 32.1	C35	15.11	5	−109.43	0.24	0.609		
21 30 54.39	+12 07 11.5	3599	16.49	4	−103.63	0.42	0.620		

NOTES.—(b): Star remains variable if jitter of 0.8 km s^{-1} is included; (j) Star is not variable if jitter of 0.8 km s^{-1} is included; (v) variable star fainter than jitter limit.

member; these are probable nonmembers. These have all been rejected from the cluster sample. These may be foreground halo dwarfs. There were also a few stars with velocities consistent with being cluster members, but the spectra were too poor to estimate the equivalent width. These have not been used in the subsequent analysis.

In Table 2, we have listed the stars deemed to be members sorted by increasing right ascension. The first two columns are our coordinates for the stars with epoch J2000.0. Column (3) contains an identification to ease cross comparisons. For the stars from the Cudworth's preliminary proper-motion list, we have used his identifications from Küstner (1921), Aurière & Cordoni (1981), or Sandage (1970). These can also be used for cross-identification with Peterson et al. (1989). For the rest of the stars we have used our own numbering from our master list of candidates. Further identification numbers for cross-referencing with Gebhardt et al. (1997) are in the penultimate column. Column (4) is a V magnitude. The remaining columns are the number of observations for each star, the mean velocities, the uncertainties in the velocities (exclusive of the uncertainty in the velocity zero point), and for each star with more than one observation, the probability that the χ^2 of the differences of the observed velocities about their mean is consistent with no variability. The final column contains any notes. The velocities of the nonmembers are available from the authors.

We have compared our coordinates with the high-precision astrometry of the inner 2′ of M15 by Le Campion, Colin, & Geffert (1996). We find mean offsets (in the sense ours − Le Campion et al. 1996) $\langle \Delta\alpha \rangle = -0\farcs68 \pm 0\farcs23$ and $\langle \Delta\delta \rangle = 0\farcs80 \pm 0\farcs22$. Since their typical error is around 0″.07, our relative astrometry is good to about 0″.2. The mean offsets represent differences in the astrometric systems used in the studies. We use the HST Guide Star Catalog as

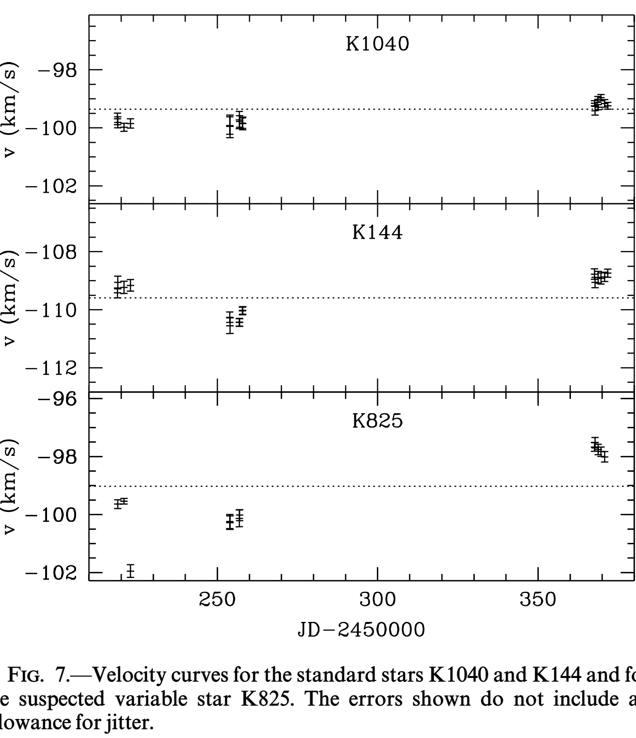

FIG. 7.—Velocity curves for the standard stars K1040 and K144 and for the suspected variable star K825. The errors shown do not include an allowance for jitter.

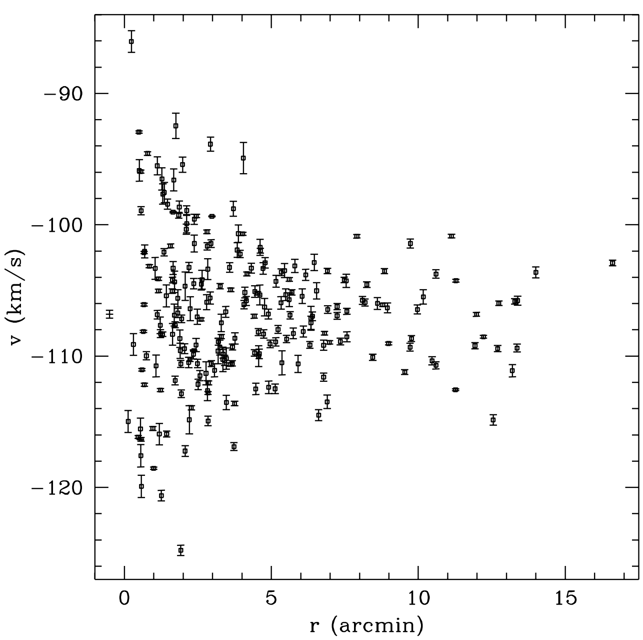

FIG. 8.—Velocities of the members of M15 plotted against radius. The velocity dispersion decreases as expected with radius until about 7′. The velocity dispersion then appears to increase again. The point at negative radius indicates the inferred mean and its uncertainty. In this case the probability distribution is symmetric.

TABLE 3

REPEAT OBSERVATIONS OF POSSIBLE VARIABLES

JD	v	ϵ_v	JD	v	ϵ_v
K92:			K825:		
2,450,218.892......	−105.87	0.43	2,450,218.962......	−99.64	0.15
2,45,0220.927......	−109.69	1.07	2,450,220.927......	−99.54	0.10
2,450,222.931......	−105.77	0.57	2,450,222.931......	−101.95	0.22
2,450,371.704......	−106.26	0.32	2,450,253.857......	−100.24	0.24
K114:			2,450,253.924......	−100.28	0.23
2,450,218.962......	−113.65	0.25	2,450,256.877......	−100.13	0.29
2,450,371.704......	−112.62	0.12	2,450,256.935......	−100.02	0.19
6607:			2,45,0367.633......	−97.67	0.15
2,450,368.778......	−95.41	1.02	2,450,367.782......	−97.52	0.18
2,450,371.704......	−104.70	0.64	2,450,368.778......	−97.76	0.18
K583:			2,450,369.603......	−97.83	0.16
2,450,253.857......	−111.97	0.30	2,450,370.753......	−98.01	0.18
2,450,371.704......	−107.77	0.09	5555:		
K706:			2,450,368.778......	−98.71	1.78
2,450,256.877......	−118.13	0.22	2,450,371.704......	−114.86	1.08
2,450,368.778......	−115.12	0.18			
K769:					
2,450,256.935......	−107.14	1.49			
2,450,371.704......	−101.88	0.94			

our reference, while Le Campion et al. (1996) use the FK5 system. The positions in the tables do not include the offset. The zero point for our photometry has been determined by comparing stars that appear in our list and that of Cudworth, and shifting our magnitudes onto his system.

There are 17 stars in our member sample for which the probability of no velocity variability is less than 1%. Of these stars, 12 are in the upper 1 mag interval of the giant branch, here for $V < 13.6$, where it has long been suspected that the stars are subject to an intrinsic "jitter" in their velocities of around 0.8 km s^{-1} (Gunn & Griffin 1979; Mayor et al. 1984; Lupton et al. 1987; Pryor et al. 1988). These include the two stars that we took as our velocity standards, K144 and K1040. Velocity curves for these two stars, plus K825, are shown in Figure 7. Both show systematic variations between runs, but the velocities are consistent if a further 0.8 km s^{-1} is allowed in the uncertainties. There are another 12 stars with two observations, six of these are at two epochs, which do not show any sign of this jitter. So it is unclear whether all bright giants suffer from this or what the timescale is of this variation. If we add 0.8 km s^{-1} in quadrature to the errors for all stars with $V < 13.6$, then three of these stars remain flagged as variables. These are marked by the note "b" in Table 2. Those with now-consistent velocities are marked "j." The other five stars are fainter than this limit and have the note "v." We provide the full set of velocities for the stars with "b" and "v" flags in Table 3. The star K673, which was claimed to be a binary by Gebhardt et al. (1994), only appears to be variable if the jitter is not included. The two observations in 1996 June and October differ by 0.8 km s^{-1}. Of the eight stars we identify as velocity variables, six have only two observations, four of which are at two epochs. The star 5555 has a velocity difference of 16 km s^{-1} over a span of 3 days; star 6607 changes by 4.3 km s^{-1} over the same interval. The most extensive set of observations is for the star K825, which was noted to be variable in our 1996 May run. We present the velocity curve in Figure 7. Most remarkable is a 2.4 km s^{-1} velocity change over the course of 2 days in our May observing run.

We will refer to the velocities without including the jitter factor as our "A" sample. This consists of 213 nonvariables and 17 variables. If we include the 0.8 km s^{-1} jitter factor in the velocity uncertainties of all the bright stars, then this "B" sample consists of 222 nonvariables and eight variables. Only the nonvariables in each sample will be used in estimating the mean, velocity dispersion profile, and rotation. In the analysis below we will use the A sample; the B sample yields very similar results.

Figure 8 displays our velocities plotted against radius. What is most striking is the apparent increase in the velocity dispersion beyond about 5′. We will discuss this point in § 4 using the methods described in § 3.

3. BAYESIAN ESTIMATION

3.1. *Introduction*

We have a sample of velocities for members of the cluster, each with its own uncertainty. What we wish to measure are the mean velocity of the cluster and the velocity dispersion profile. The mean must be based on all the velocities, but the velocity dispersion needs to be measured as a function of radius, e.g., in radial bins. In addition, we often want to know whether the observations indicate rotation and whether the rotation signal is significant. There are several approaches of increasing complexity that can be used to make these various measurements.

Peterson et al. (1989) used the simplest approach to calculating the mean and simply took an unweighted average of their 120 stellar velocities and derived the uncertainty from the scatter about the mean. This overstates the uncertainty, since it will also include the unknown velocity dispersion of the cluster. They determined the velocity dispersion profile by dividing the sample into bins and taking the dispersion about the mean of the velocities in that bin as the local velocity dispersion. Again, the known and variable uncertainties in the velocities are ignored. Furthermore, the estimate of the cluster velocity based on the entire sample has also been ignored in determining the local velocity dispersion. The fractional error in the velocity dispersions was just taken as $(2N)^{-1/2}$ for a bin of N stars.

A more sophisticated approach is the maximum likelihood method described by Pryor & Meylan (1993). This assumes that the velocity for each star is drawn from a normal distribution with the standard deviation being the quadrature sum of the individual velocity uncertainty and the cluster velocity dispersion. Standard maximum likelihood techniques result in equations for the mean and dispersion, which can then be solved numerically. Pryor & Meylan (1993) also give equations for the variances of the derived quantities.

Another algorithm that has been used to measure the velocity dispersion profile utilizes the locally weighted scatter plot smoothing (LOWESS) algorithm (Cleveland & McGill 1984). First the cluster mean is estimated by some other method. Then the velocity variance at each data point is estimated according to the application of this algorithm by Gebhardt et al. (1994). The squared deviations from the cluster mean are calculated. Then, at each radius for which one wants to measure the dispersion, one proceeds as follows: (1) A straight line is fitted to these deviations as a function of radial position by weighted least squares. The weights are the inverse squares of the differences of the stars in radial position, measured from the cluster center, with respect to the dispersion radius. (2) The square root of the fitted variance is taken as the velocity dispersion at that radius. The uncertainties in the velocity dispersions are calculated using a Monte Carlo method that assumes that the LOWESS dispersions are correct, but using the observed velocity uncertainties for individual stars. While this method does yield a nonparametric estimate of the velocity dispersion profile, it suffers from calculating the mean and dispersions separately and from ignoring the measurement errors in calculating the velocity dispersion. Thus, all velocities carry equal weight and the measurement of the velocity dispersion can be biased by single, highly uncertain points with large deviations. To some extent this will be compensated for in estimating the uncertainty in the velocity dispersions, and more recent applications of the method have included the velocity uncertainty in the weighting (K. Gebhardt, 1997 private communication), but the robustness of this method has not been demonstrated.

Looking at the maximum likelihood method from another perspective brings us to the Bayesian methods we employ here. The results are generally similar to those achieved with maximum likelihood, but there are several advantages. The Bayesian methods give probability distributions for the parameters, not just the most likely value and its variance. The Bayesian methods naturally incorporate any prior information on the values to be measured and also give the relative likelihood of various models. Thus, for example, we can decide whether a model including rotation is more or less likely than one without.

For discussions of the background of Bayesian analysis, we refer the reader to Bretthorst (1988) and Press (1989). The classic source is Jeffreys (1961). Jaynes (1983) presents this material from a more modern perspective. Saha & Williams (1994) have used these methods in a somewhat different astronomical context.

In short, if we know the conditional probability of A given B, $P(A \mid B)$, then we can infer $P(B \mid A)$ using Bayes's theorem,

$$P(B \mid A) = \frac{P(A \mid B)P(B)}{P(A)} . \quad (2)$$

In equation (2), $P(B)$ is referred to as the *prior probability* or the *prior*. It represents any information we have on the values of the parameters before we look at our data. $P(A \mid B)$ is the *likelihood*. $P(B \mid A)$ is the *posterior probability*; it is this that we are seeking to measure. The final factor, $P(A)$, is called the *global likelihood* and is a normalization factor.

A and B can represent data, models, model parameters, and so on. In a Bayesian framework, the probabilities represent our state of knowledge. This is unlike the more familiar "frequentist" viewpoint, which considers probabilities to be just the frequency with which something occurs. Here it is perfectly meaningful to discuss the probability of the parameters of a model having particular values. It is just as meaningful to compare the probability of two models. The question is not, "How often will such a model occur?" but rather "Given the previously known information and the data, what is the probability that this model is correct?" The prior represents our state of knowledge before making the observation. We may know nothing at all, in which case we would wish to choose as uninformative a prior as possible. Alternatively, we may have previous measurements that we are trying to refine. In this case, the proper prior is one that represents the previous measurements. We will see examples of both of these kinds of prior below. The appendices to Bretthorst (1988) contain some useful comments on the choice of priors.

If we have two different models, M_1 and M_2, and we wish to choose between them, then the natural thing to look at is the posterior odds ratio

$$\frac{P(M_1 \mid D)}{P(M_2 \mid D)} = \frac{P(D \mid M_1)P(M_1)}{P(D \mid M_2)P(M_2)} , \quad (3)$$

where D is the data. If the number or nature of the parameters in the two models differ, it is important to keep all the normalization terms in the priors and likelihoods. If the odds ratio is greater than unity, then model M_1 is favored; otherwise, model M_2 is more likely. This will be used in discussing rotating and nonrotating models for the M15 data.

Since the notion of a posterior odds ratio is unfamiliar, we feel that some further discussion is warranted to give a proper understanding of our results. Assume that $P_1(M_1 \mid D)$ and $P_2(M_2 \mid D)$ are the probability distributions for the values of two parameters, M_1 and M_2, given the data, and further, assume that they are normal distributions with means μ_i and dispersions σ_i, where $i = 1, 2$. We can calculate the probabilities that $M_1 > M_2$ or that $M_1 < M_2$ and hence the odds of the two propositions. Define $k \equiv (\mu_1 - \mu_2)/(\sigma_1^2 + \sigma_2^2)^{1/2}$. Then the odds of $M_1 > M_2$ over $M_1 < M_2$ are

$$[1 + \mathrm{erf}\,(k/\sqrt{2})]/[1 - \mathrm{erf}\,(k/\sqrt{2})] .$$

If $\mu_1 = \mu_2$, then $k = 0$ and the odds are even; the two propositions are equally likely. For $k = 1$, a 1 σ result, the odds are 5.3 to 1. That is, based on our prior knowledge and this data set, it is 5.3 times more likely that $M_1 > M_2$ than $M_1 < M_2$. If μ_1 is 2 σ larger than μ_2, the odds of $M_1 > M_2$ over $M_1 < M_2$ are 43 to 1. Similarly, $k = 3$ gives odds of 740 to 1. If a horse in a race has odds of 5 to 1 against its winning, you would not be surprised if it won. Similarly, if the posterior odds are 5 to 1 against M_2 being larger than M_1, you would not be surprised if it really was larger. In general, we do not think of a 1 σ result as being overly significant. If the odds were 740 to 1, we would be surprised if the horse won or if, with additional data, M_2 proved to be larger than M_1. But we are similarly surprised if a 3 σ result proves to be wrong. Nonetheless, it can be, and long shots do sometimes win.

3.2. *Velocity Models and Priors*

Here we will look at several models for a globular cluster data sample, with different assumptions about the form of the velocity dispersion profile and about whether the cluster is rotating. The first pair of models assumes a single mean velocity for the sample and then individual velocity dispersions for groups of stars binned by radius. The sizes of the bins are variable; we assume only that the velocity dispersion is the same for all stars in that radial bin. In effect, we assume that the velocity dispersion can be approximated by a series of step functions. This is a general assumption of binning. First we will consider a model without rotation.

The data sample consists of N stellar velocities v_i, each with uncertainty ϵ_i. The model parameters are the mean velocity $\bar{v}$ and the set of velocity dispersions σ_r for the $r = 1, \ldots, M$ radial bins. For a single observation, we assume that the likelihood of observing v_i is given by

$$P(v_i \mid \bar{v}, \sigma_r, \epsilon_i) = \frac{1}{\sqrt{2\pi(\epsilon_i^2 + \sigma_r^2)}} \exp\left[-\frac{(v_i - \bar{v})^2}{2(\epsilon_i^2 + \sigma_r^2)}\right]. \quad (4)$$

The likelihood of the whole data set D is

$$P(D \mid \bar{v}, \{\sigma_r\}, \{\epsilon_i\}) = \prod_i P(v_i \mid \bar{v}, \sigma_r, \epsilon_i) . \quad (5)$$

Applying equation (2) yields

$$P(\bar{v}, \{\sigma_r\} \mid D, \{\epsilon_i\}) \propto P(D \mid \bar{v}, \{\sigma_r\}, \{\epsilon_i\}) P(\bar{v}) \prod_r P(\sigma_r) \quad (6)$$

for the posterior probability. We have ignored the normalization factor $P(D)$, as we will only be concerned with the relative probabilities of various parameter combinations and, for different models of the same data, $P(D)$ is constant.

$P(\bar{v})$ and $P(\sigma_r)$ are the priors for the mean velocity and the velocity dispersion values. If we know nothing about the mean velocity, then the appropriate prior to use is a uniform prior. In one sense, this is a somewhat unusual probability distribution in that it is not normalizable. In practice, this is not usually a problem. If we have a previous observation of the mean $\bar{v}_0 \pm \sigma_{\bar{v}0}$, then we could use a normal distribution

$$P(\bar{v}) = \frac{1}{\sqrt{2\pi}\sigma_{\bar{v}_0}} \exp\left[-\frac{(\bar{v} - \bar{v}_0)^2}{2\sigma_{\bar{v}_0}^2}\right] \quad (7)$$

for the prior. The appropriate uninformative prior for a scale parameter such as the velocity dispersion σ_r is the Jeffreys (1961) prior σ_r^{-1} (for a justification, see Bretthorst 1988).

An alternative model is one which allows for rotation in the data in addition to the mean and dispersion as in the previous model. One simple model is to assume a sinusoidal dependence of rotation velocity on azimuthal angle with a single position angle ϕ_0 and amplitude A. We replace equation (4) with

$$P(v_i, \phi_i \mid \bar{v}, \sigma_r, \phi_0, A, \epsilon_i) = \frac{1}{\sqrt{2\pi(\epsilon_i^2 + \sigma_r^2)}} \times \exp\left(-\frac{\{v_i - [\bar{v} + A \sin(\phi_i - \phi_0)]\}^2}{2(\epsilon_i^2 + \sigma_r^2)}\right), \quad (8)$$

where ϕ_i is the position angle for observation i. The posterior probability is then

$$P(\bar{v}, \{\sigma_r\}, \phi_0, A \mid D, \{\epsilon_i\}) \propto P(D \mid \bar{v}, \{\sigma_r\}, \phi_0, A, \{\epsilon_i\}) \times P(\bar{v}) P(\phi_0) P(A) \prod_r P(\sigma_r) . \quad (9)$$

The appropriate choice for the new priors is discussed in Bretthorst (1988). Based on his discussion, we use

$$P(\phi_0) P(A) = \frac{1}{2\pi\delta^2} \exp\left(-\frac{A^2}{2\delta^2}\right). \quad (10)$$

The pseudodispersion δ is a *hyperparameter*. This is a case in which we cannot use an improper, i.e., nonnormalizable, prior, as we want to compare the probabilities of the model with and without rotation. The other parameters with improper priors are common to both models, so their normalization divides out. The rotation parameters are only in one model, and so their normalization must be taken into account for a proper comparison. We can see in the raw data (Fig. 12 below) that any rotation for M15 must be small. This sets a limit on δ. The value we choose for δ expresses our estimate of the maximum amplitude of the rotation; the greater a value we assign to δ, the larger the rotation signal must be to be considered significant with respect to the model without rotation.

As an alternative to a step function for the velocity dispersion profile, we can consider a power-law form:

$$\sigma(r) = \sigma_0 r^{\alpha} . \quad (11)$$

This is still parametric, but does away with binning. The likelihood for a single observation is now

$$P(v_i \mid \bar{v}, \sigma_0, \alpha, \epsilon_i) = \frac{1}{\sqrt{2\pi(\epsilon_i^2 + \sigma_0^2 r^{2\alpha})}} \times \exp\left[-\frac{(v_i - \bar{v})^2}{2(\epsilon_i^2 + \sigma_0^2 r^{2\alpha})}\right], \quad (12)$$

and the posterior probability is

$$P(\bar{v}, \sigma_0, \alpha \mid D, \{\epsilon_i\}) \propto P(D \mid \bar{v}, \sigma_0, \alpha, \{\epsilon_i\}) P(\bar{v}) P(\sigma_0) P(\alpha) . \quad (13)$$

The new priors are given by $P(\sigma_0) = \sigma_0^{-1}$, the Jeffreys prior referred to above, and

$$P(\alpha) = \frac{1}{\sqrt{2\pi}\gamma} \exp\left[-\frac{(\alpha - \alpha_0)^2}{2\gamma^2}\right]. \quad (14)$$

As in equation (10), α_0 and γ are hyperparameters. Theory suggests $\alpha_0 = -0.5$, and we take $\gamma = 1$. The extension to the rotating case is straightforward.

3.3. *Metropolis Algorithm*

We calculate the posterior probability distributions using the Metropolis algorithm and follow the procedure in Saha & Williams (1994). The basic algorithm is as follows: We will refer to a set of parameters as ϖ. (1) Start with some values of the parameters ϖ and calculate the posterior probability $P(\varpi \mid D)$. (2) Pick at random from a uniform distribution a possible change $\delta\varpi$ in the parameters and compute $P(\varpi + \delta\varpi \mid D)$. (3) If $P(\varpi + \delta\varpi \mid D) > P(\varpi \mid D)$, then replace ϖ with $\varpi + \delta\varpi$ for the next iteration. If not, replace ϖ with $\varpi + \delta\varpi$ with probability $P(\varpi + \delta\varpi \mid D)/P(\varpi \mid D)$. (4) Return to step 2 and iterate. The size of the trial changes must be large enough to ensure that the entire range of acceptable values of the parameters are covered, but be small enough that sufficient iterations accept change. Given enough iterations, the distribution of accepted values for the parameters converges into the posterior probability distribution.

In principle, we should save each set of parameters to look at the full, multivariate distribution, but this would require too much memory and require too many iterations if the number of parameters is much larger than two. What we have done instead is to save the distribution of each parameter individually. This is equivalent to projecting the multivariate distribution along the axis of each parameter, that is, simultaneously calculating all the marginal probability distributions. Our estimator for each parameter is then the mode of the individual probability distribution. The posterior probability of the model is given by the overall probability using these estimators of the modes. With some multivariate probability distributions, it is possible for the peaks of the projected distributions to be significantly different from the global peak of the distribution. To help guard against this, we also keep track during the iterations of the individual parameter sample giving the highest posterior probability. In general, this set of parameters was close to, but not identical with, the modes of the individual distributions; the posterior probabilities were similar. In practice, the distributions from our data sets are unimodal and strongly peaked, indicating that the modes of the projected distributions do represent fairly the peak of the multivariate distribution.

These projected posterior probability distributions for the various parameters were measured by counting the number of accepted parameter values on a grid. For a parameter x, $P_i \Delta x$ is the probability of x being between x_i and $x_i + \Delta x$, where the x_i are the grid points. We calculate the mode of $P(x \mid D)$ by finding the maximum value of P_i, at e.g., x_j, and then using it and the two bracketing values to find the parabola $y(x)$ for which $\int_{x_i}^{x_i+\Delta x} y(x)dx = P_i \Delta x$ for each of $i = j-1, j, j+1$. The maximum of $y(x)$ is taken as the mode of the distribution. Using this interpolation form, the mode lies at

$$x = x_{j-1} + \frac{2P_{j-1} - 3P_j + P_{j+1}}{P_{j-1} - 2P_j + P_{j+1}} \Delta x . \quad (15)$$

The number of iterations and the grid spacings for each parameter were chosen to ensure a smooth, well-sampled distribution. Generally we used of order 10^6 samples to derive the posterior distributions.

3.4. *Examples*

We conclude this discussion with a couple of examples to demonstrate this method. For our first example, we draw a sample of stars with the radii and errors of our "A" sample. The velocities are drawn from a distribution with a mean velocity of -107 km s^{-1} and with a velocity dispersion profile that decreases linearly to 6′, and then is constant beyond that, similar to the observed velocity dispersion profile. We then use the same parameters as in § 4 to analyze this sample. The results are shown in Figure 9. The dotted line is the assumed profile. The estimates of the velocity dispersions are displayed in two ways on this diagram: points with error bars and sideways histograms representing the probability distribution; the former displays the values in a traditional manner. The data points represent the mode of the distribution as discussed in § 3.3. The error

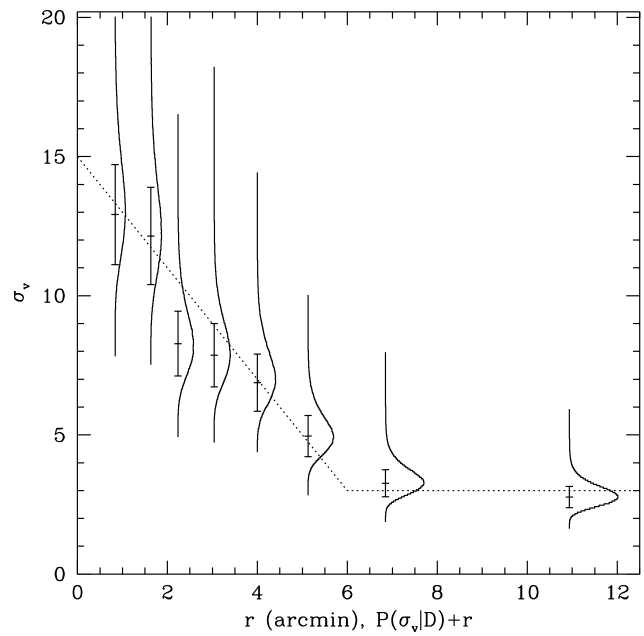

FIG. 9.—Velocity dispersion profile for the first example. The assumed velocity dispersion profile is shown as the dotted line. The histograms (turn the figure sideways) show the probability distributions for the velocity dispersion at that radius having the given value. The probability distributions are offset to have their zero levels at the mean radius of the star in the bin. This is the same position as the vertical line of the error bars for the accompanying points. The points represent the modes of the probability distribution and the error bars the symmetric region containing 68.5% of the probability. These can be thought of as 1 σ error bars. Note that the probability distribution is really asymmetric; it is skewed to higher velocity dispersions. There is good agreement between the assumed profile and the estimated profile from the artificial data.

bars represent the symmetric region about the mode over which the integrated probability is 0.685. Thus, they are equivalent to 1 σ errors. Note, however, that a symmetric probability integral is only one way of selecting the error region. Any contiguous region containing 68.5% of the probability would be equivalent. The agreement of the derived velocity dispersion profile with that assumed is quite satisfactory, and the inferred mean velocity is -107.0 ± 0.3 km s^{-1}.

For our second example, we draw the stars as before but also assume the entire cluster is rotating with amplitude 2 km s^{-1} and a position angle of 180°. We analyzed this result with both the rotating and nonrotating models. The rotation is estimated to have an amplitude of 1.7 ± 0.5 km s^{-1} and position angle $176° \pm 19°$. The mean is -106.7 ± 0.3 km s^{-1}. These all agree with the input model. The velocity dispersion profile is shown in Figure 10. There is general agreement between the estimates of the velocity dispersion and the assumed values. The model including rotation is a more likely fit to the data, with odds of 10 to 1 in favor of rotation. This is only marginally significant, as the data do not strongly support an interpretation of rotation. The sixth point may appear to be too low, but full consideration of the statistics indicates that this is not the case. The advantage of having the full probability distribution becomes apparent if we consider the odds ratio for this point to be greater or less than the assumed value at that radius. If we naively ignore the asymmetry and assume the probability distribution to have the mean and standard deviation shown, the difference is 2.5 σ, and the odds against the true

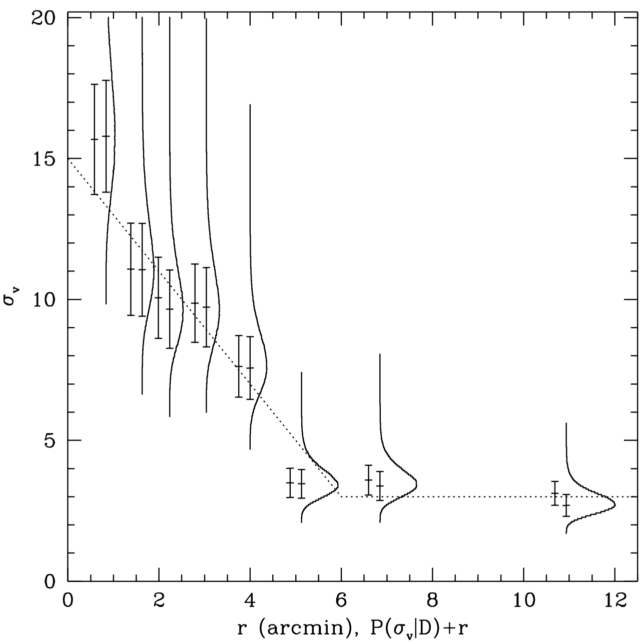

FIG. 10.—Velocity dispersion profile for the second example. The assumed velocity dispersion profile is shown as the dotted line. The curves and points are as described in Fig. 9, except that we also show the mode and error bars for the solution without rotation. These are offset to the left.

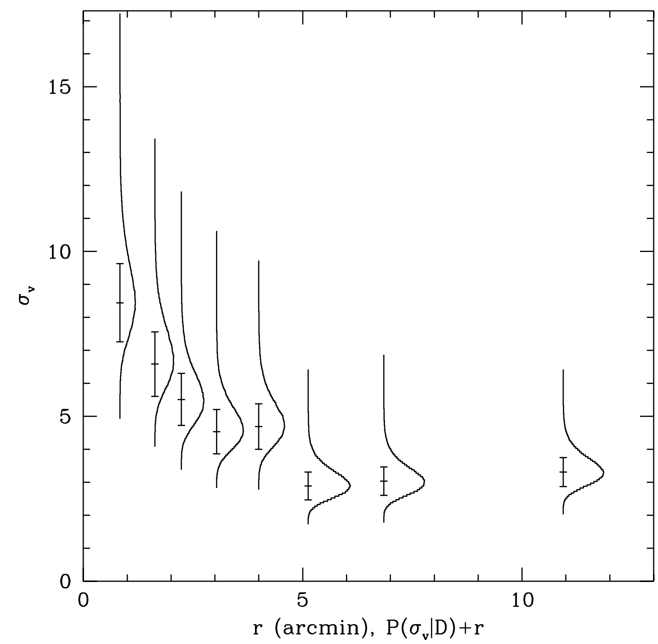

FIG. 11.—Inferred velocity dispersion profile assuming no rotation. The curves and points are as described in Fig. 9.

value being higher than the assumed value are 173 to 1. If we use the measured probability distribution, the odds are only 31 to 1, 5.5 times less unlikely, and equivalent to a 1.3 σ difference for normally distributed errors.

4. KINEMATICS

4.1. *Velocity Dispersion Profile*

We now apply to our observations the methods discussed in § 3. We begin by assuming that the cluster is not rotating. We divide the A sample into seven bins of 26 stars each and an outermost bin of 31 stars, and run it through the Bayesian analyzer. The resulting mean velocity is -106.9 ± 0.3 km s^{-1}, assuming a uniform prior and -107.3 ± 0.2 km s^{-1} if we use the Gebhardt et al. (1997) mean and uncertainty (-107.8 ± 0.3 km s^{-1}) as the prior. Our result in the latter case is just the average of the two measurements, exactly as we would have expected. The probability distribution of the mean velocity is well represented by a normal distribution with the quoted mean and dispersion.

Figure 11 illustrates the resulting velocity dispersion profile in the outer part of the cluster. If we use the B sample and just add the "jitter" stars into the same radial bins, the results are much the same. The points and curves are as described for the examples in the previous section. The modes and the size of the symmetric error region are listed in Table 4. The radius given in the leftmost column is just the mean radius of the stars in the bin. The histograms give the actual probability distributions for each velocity dispersion. These can be seen more clearly by turning the figure sideways. The zero level for the probability for each bin is the mean radius of the stars in the bin as represented by the vertical stroke of the error bars. It is clear that the probability distributions are skewed in all cases to higher velocity dispersions. It is more likely that the true dispersion is higher, rather than lower, than the mode. This is easy to understand. It is always possible that the observed sample of stars lacks stars with large velocity differences from the mean, even if the underlying velocity distribution allows for such values. On the other hand, the stars with the largest velocity deviations in the sample put a much stronger lower limit on the velocity dispersion.

With the exclusion of the point at 4′, the velocity dispersion decreases with radius up to 5′. Beyond this radius, the modes of the distributions increase again, confirming what is seen in the raw velocities. Since we have computed the probability distributions, it is straightforward to calculate the probability that one point is larger than another, or, alternatively, the odds. The probability that the last point is higher than the next-to-last point is 67%, i.e., the odds are roughly 2 to 1 in favor of the last point being higher. For the last point and the point at 5′, the probability that the last is larger is 74%, giving odds of 2.8 to 1. (For an explanation of these odds ratios, see § 3.1.) While intriguing, these results do not in themselves argue strongly for an increase in the velocity dispersion.

4.2. *Rotation*

It could be argued that the increase in the velocity dispersion is the result of differences in the velocity tensor with

TABLE 4

VELOCITY DISPERSION PROFILE

RADIUS (arcmin)	σ (km s^{-1})	
	No Rotation	Rotation
0.83	8.1 ± 1.2	7.8 ± 1.1
1.64	6.1 ± 0.9	5.8 ± 0.9
2.23	6.3 ± 1.0	6.5 ± 0.9
3.04	4.5 ± 0.7	4.5 ± 0.7
4.00	4.7 ± 0.7	4.2 ± 0.6
5.14	2.9 ± 0.4	3.0 ± 0.5
6.86	3.0 ± 0.5	2.8 ± 0.4
10.94......	3.2 ± 0.5	3.3 ± 0.4

radius. If the velocities are strongly tangentially anisotropic, the projected velocity dispersion would be higher than if the velocities are isotropically distributed. We discuss the case against tangential anisotropy in § 5, but since rotation has been claimed in the past for M15, here we look further at the special case of rotation. Gebhardt et al. (1997) find rotation with an amplitude of 2.1 ± 0.4 km s^{-1} and position angle $107° \pm 10°$ for their overall sample.[4] They also look at the variation with radius and find changes in both the amplitude and position angle.

Before continuing on to look for rotation in our sample, we need to address the question of "perspective rotation" arising from the proper motion of M15. This is discussed by Feast, Thackeray, & Wesselink (1961) and more specifically with respect to ω Centauri by Merritt, Meylan, & Mayor (1997). Simply put, the projection of the cluster's space velocity along the lines of sight to various parts of the cluster results in an apparent rotation of the cluster, increasing with distance from the cluster center and varying inversely with the cluster distance. For ω Cen, which is at 5.2 kpc and has a total proper motion of 0ʺ.78 (100 yr)$^{-1}$, the perspective rotation is about 1 km s^{-1} at 20′. M15 is at 10.5 kpc; the value of its proper motion is disputed. Cudworth & Hanson (1993) measured an absolute proper motion of $\mu_\alpha \cos \delta = -0.''03 \pm 0.''10$ (100 yr)$^{-1}$, $\mu_\delta = -0.''42 \pm 0.''10$ (100 yr)$^{-1}$. Geffert et al. (1993) measured it to be $\mu_\alpha \cos \delta = -0.''10 \pm 0.''14$ (100 yr)$^{-1}$, $\mu_\delta = -1.''02 \pm 0.''14$ (100 yr)$^{-1}$. More recently Scholtz et al. (1996) derived a value of $\mu_\alpha \cos \delta = -0.''01 \pm 0.''04$ (100 yr)$^{-1}$, $\mu_\delta = +0.''02 \pm 0.''03$ (100 yr)$^{-1}$. None of these values agree, and the latest is effectively zero. Hence, we will ignore the effects of perspective rotation here.

If we use the rotating model for the velocities discussed in § 3.2, assuming a single amplitude and position angle for the whole sample, then the mean velocity is the same. We have taken the hyperparameter δ (see § 3.2) to be 5 km s^{-1}. Rotation is detected. The amplitude is 1.5 ± 0.4 km s^{-1} and the axis of rotation is at $125° \pm 19°$. The posterior odds ratio for a rotating model with respect to a nonrotation model is 15 to 1, indicating that the rotating model is more likely. This rotation is displayed in Figure 12. The corresponding velocity dispersion profile, corrected for rotation, is shown in Figure 13. For comparison, the modal values for the nonrotating analysis are shown as horizontal dashes offset to slightly smaller radii. Again, the modes and sizes of the symmetric error regions are given in Table 4. Rotation, if present, acts to increase the observed velocity dispersion if not accounted for. The large decrease in the velocity dispersion for the 4′ point indicates that it is the stars at this radius that are most strongly affected by rotation. The dispersion at 7′ also decreases somewhat for the rotating model. The probability that the last point is higher than the next to last is now 77%, i.e., the odds are roughly 3.3 to 1 in favor of the last point being higher, somewhat higher than for the case without rotation. For the last point and the point at 5′, the probability that the last is larger is now only 65%, giving odds of 1.8 to 1. The velocity dispersion now appears to reach its minimum closer to 7′, rather than at 5′ as in Figure 11.

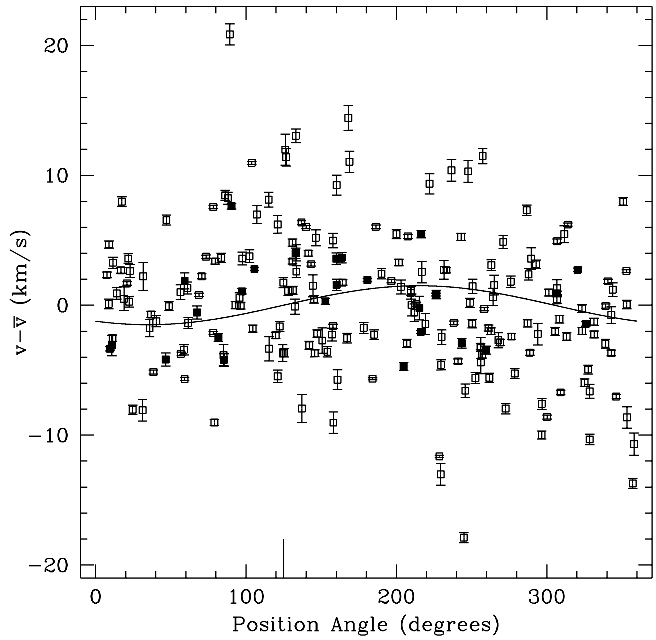

FIG. 12.—Observed velocities, less the cluster mean, as a function of position angle measured eastward from north. The inferred rotation is shown as the curve. The position angle of the rotation axis is indicated by the large tick mark. The stars in the 4′ bin, which has the most significant rotation, are shown as filled symbols.

Since it has been claimed by Gebhardt et al. (1997) that the rotation properties change with radius, we have reanalyzed our sample by looking for rotation in each of our bins separately. We have kept the mean velocity fixed at -106.9 km s^{-1}. The results are shown in Table 5. Unlike Table 4, each bin is analyzed separately in this table. For each bin, as well as the overall sample analyzed in one bin

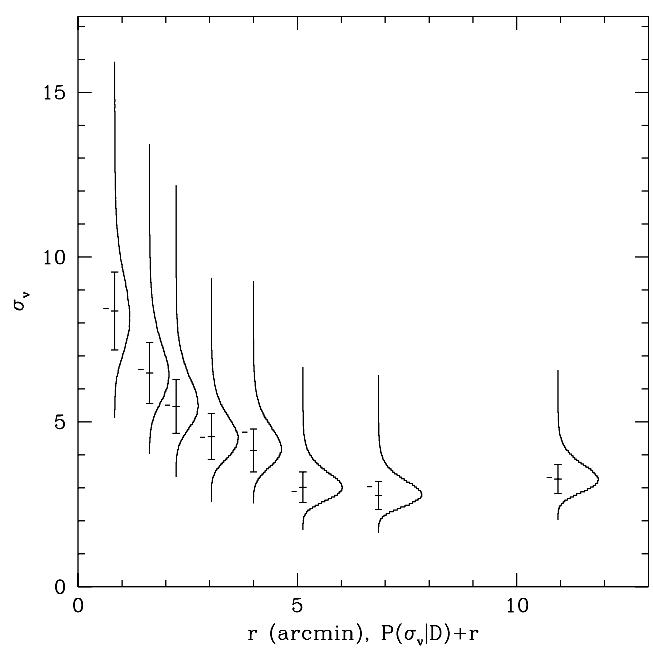

FIG. 13.—Same as Fig. 10 for the velocity dispersion profile, but assuming there is rotation. The dispersion values from Fig. 11 are shown as tick marks offset to the left of the new points. Note the decrease in the dispersion at 4′.

[4] Gebhardt et al. (1997) define their position angle as the velocity maximum. We define ours as the rotation axis with the direction defined by right-handed rotation about it. We have subtracted the required 90° from their values to bring the definitions into agreement.

TABLE 5

RESULTS BY INDIVIDUAL BINS

	No Rotation	Rotation			
Radius (arcmin)	σ (km s^{-1})	σ (km s^{-1})	A (km s^{-1})	ϕ	P(rot.)/P(no rot.)
0.83	8.2 ± 1.2	7.5 ± 1.1	4.3 ± 2.1	141 ± 34	0.08
1.64	6.3 ± 0.9	5.9 ± 1.0	3.1 ± 1.9	174 ± 40	0.07
2.23	6.2 ± 1.0	6.3 ± 1.0	<2.4	...	0.01
3.04	4.5 ± 0.7	4.4 ± 0.7	<2.6	...	0.02
4.00	4.6 ± 0.7	3.9 ± 0.6	3.3 ± 1.2	103 ± 22	1.2
5.14	3.0 ± 0.4	3.0 ± 0.4	<1.1	...	0.01
6.86	3.0 ± 0.5	3.0 ± 0.4	1.2 ± 0.8	106 ± 47	0.03
10.94	3.2 ± 0.4	3.3 ± 0.5	<1.1	...	0.01
All	5.2 ± 0.3	5.1 ± 0.3	2.0 ± 0.5	131 ± 17	26

(the row marked "All"), we give the dispersion without rotation and the dispersion, rotation amplitude, and position angle assuming rotation. The final column gives the posterior odds ratio in the sense $P(\text{rotation}\,|\,D)/P(\text{no rotation}\,|\,D)$. Values larger than 1 indicate the model with rotation is more likely. For the bins in which no rotation is detected, i.e., those with near-zero amplitudes, the errors are the amplitude at which the integrated probability reaches 0.685, which corresponds to a 1 σ upper limit. The only bin in which there is significant rotation detected is the one at 4′, as we expected. The stars in this bin are highlighted in Figure 12. For a different binning, one with six bins alternating with 35 or 36 stars, no single bin shows significant rotation individually, yet the combined solution has posterior odds in favor of rotation of 33 to 1.

The proceeding results can be explained as a consequence of a subset of the observed velocities combining together to give the rotation signal. These stars are distributed across many of the bins and, depending on the binning, a given radial range may or may not show the rotation signal. What the Bayesian posterior odds ratio gives is the strength with which one model is preferred over the other. In the last mentioned case, the rotating model with six bins is 33 times more likely to be a true description of the data than the nonrotating model with six bins. Similarly, for the original eight-bin model, the rotating model is about 15 times more likely than the nonrotating model. These are the same data; why the difference? This is a result of the interaction between the velocities of the stars in each bin and the dispersion and overall rotation in the model. Experiments with selections of radial subsamples show that a group of 32 stars, including all of those in the 4′ bin above, have a strong probability of rotation. In the six-bin model, these stars are divided into two bins and are combined with radially adjacent stars, which do not support the rotation hypothesis as strongly. The individual bins do not show high probabilities of rotation, but the entire sample retains the signal. A recent Fokker-Planck study of rotating globular clusters shows that the rotation velocity should peak at an intermediate radius (Einsel & Spurzem 1997). Since the rotation amplitude is small, we would expect to detect it only where it is the strongest.

We conclude that our sample supports the view that rotation is present in M15. This rotation appears strongest near 4′, but stars from the entire sample contribute to the signal. The sample is not large enough to look for radial changes in the rotation amplitude or position angle in a way independent of the binning. The ambiguities introduced by binning, characteristic of such a parametric approach, suggests that a nonparametric method would be a better way to resolve this question. In either case, more data are required.

Even if M15 does rotate, the amplitude is small and little rotation appears to occur outside 5′, i.e., in the region in which the velocity dispersion increases. Thus, rotation cannot explain the increase in the velocity dispersion.

5. DISCUSSION

Our observations of velocities in M15 indicate that the velocity dispersion reaches a minimum at a radius of around 7′ and then appears to increase beyond this radius. Even if it does not increase, and the current data do not unequivocally require an increase, it is unlikely that the velocity dispersion continues to decrease at the rate expected for an isolated cluster. On theoretical grounds, we would expect the velocity dispersion to decrease with radius as a power law for an isolated cluster, $\sigma(r) = \sigma_0 r^{\alpha}$, with a power-law index close to $\alpha = -0.5$.

To test this, we have used the Bayesian algorithm to fit a model assuming a power-law relation for the velocity dispersion rather than the step function (i.e., a profile that is constant across each bin) used above. This model is also discussed in § 3. We have excluded the 31 stars in the final bin from the fit. For the model without rotation, $\alpha = -0.46 \pm 0.08$, and for the model with rotation, $\alpha = -0.48 \pm 0.08$. In both cases, $\sigma_0 = 7.7$. For the 31 stars in the final bin, we calculated the posterior probabilities for the single-dispersion and power-law models, and hence the posterior odds ratio. Both without and with rotation, the dispersion calculated by the step-function model is favored for the last bin. The odds against the power-law model are 165 to 1 without rotation and 320 to 1 with rotation.

This finding strongly suggest that there is an external energy source that heats the outer regions of the cluster and causes the observed deviation of the velocity dispersion profile from power-law behavior in the outermost part of the cluster. The most likely and expected energy source is tidal interaction with the Galaxy. Whether the observed heating is due to the general Galactic tide or is due to shocks involving disk or bulge passages is impossible to say, given the current state of the observations and models.

But is an energy source necessary? While rotation has been ruled out, it could be argued that unorganized, *tangential* anisotropy could produce the observed behavior of the velocity dispersion. This seems unlikely. Tonry (1983) has computed the velocity dispersion profile for spherical galaxies of varying anisotropy. Even for extreme tangential anisotropy, there is an increase in the velocity dispersion only inside the effective radius of an $r^{1/4}$ law. Beyond this point, the velocity dispersion decreases whatever the degree of anisotropy. Thus it is difficult to see how tangential anisotropy can increase the velocity dispersion in the outermost region of a globular cluster. Further, modeling of isolated globular clusters clearly demonstrates that the outer parts of such clusters would be strongly *radially* anisotropic (Larson 1970; Spitzer & Shull 1975; Cohn 1979). To convert this to tangential anisotropy would require external forces: those originating with the host galaxy. Thus, the explanation of tangential anisotropy, even if it could provide an increase in the velocity dispersion, and Tonry's results suggest otherwise, still requires the influence of the galactic tidal field to change the orbits of the cluster stars. To convert radial orbits to circular orbits at the same apocenter requires energy input, i.e., tidal heating.

The increase in the velocity dispersion that we observe in the outer part of M15 is qualitatively very similar to that seen in the models of Allen & Richstone (1988). Their results suggest that the tidal radius should be identified as the location of the minimum velocity dispersion, at a radius of 7′, which is very different from the 23′ tidal radius measured by Grillmair et al. (1995). It is premature, however, to draw firm conclusions, since the theory of tidal heating and shocking has advanced since Allen & Richstone (1988). In particular, the recognition of the importance of the second-order effects (Kundić & Ostriker 1995) and the new appreciation of the limitations of the assumption of adiabatic invariance (Weinberg 1994) require new models. Such modeling is well within current computational capabilities. What are required are models that can be compared with observations. If new models support the idea that the minimum in the velocity dispersion marks the edge of the region containing most of the bound stars, then our results are indeed in contradiction with the analysis of the surface density profile by Grillmair et al. (1995).

Besides new models, additional observations are also required in order to improve the statistical significance of our results and to clarify the role of rotation. We have observed virtually all the stars on the giant branch brighter than $V = 16.6$ outside the central region and inside 18′. Below this magnitude, confusion with the Galactic field becomes much stronger. Further out, the fraction of members is similarly lower. While Hydra is an efficient instrument for observing large numbers of stars, better selection criteria based on, e.g., metallicity discriminating photometry using the Washington or DDO systems, are required. We have made such observations on the Washington system for the globular cluster M92, resulting in a striking increase in the fraction of stars in the sample selected for Hydra observation proving to be members. These observations will be presented in a future paper.

We thank K. Cudworth for the list of stars in his proper-motion program in advance of publication. We appreciate the support of grants from the Indiana University College of Arts and Sciences and Office of Research, and the University Graduate School. B. W. M. was supported by a grant from the Holcomb Research Institute at Butler University.

REFERENCES

Aguilar, L., Hut, P., & Ostriker, J. P. 1988, ApJ, 335, 720
Allen, A. J., & Richstone, D. O. 1988, ApJ, 325, 583
Aurière, M., & Cordoni, J. P. 1981, A&AS, 46, 347
Bretthorst, G. L. 1988, Bayesian Spectrum Analysis and Parameter Estimation (New York: Springer)
Capriotti, E. R., & Hawley, S. L. 1996, ApJ, 464, 765
Cleveland, W., & McGill, R. 1984, J. Am. Stat. Assoc., 79, 807
Cohn, H. 1979, ApJ, 234, 1036
Cudworth, K. M., & Hanson, R. B. 1993, AJ, 105, 168
De Marchi, G., & Paresce, F. 1994, ApJ, 422, 597
———. 1995, A&A, 304, 202
Drukier, G. A. 1995, ApJS, 100, 347
Drukier, G. A., Cohn, H. N., Lugger, P. M., & Yong, H. 1997, ApJ, submitted
Dubath, P., Meylan, G., & Mayor, M. 1994, ApJ, 426, 192
Dull, J. D., Cohn, H. N., Lugger, P. M., Murphy, B. W., Seitzer, P. O., Callanan, P. J., Rutter, R. G. M., & Charles, P. A. 1997, ApJ, 481, 267
Einsel, C., & Spurzem, R. 1997, MNRAS, submitted
Feast, M. W., Thackeray, A. D., & Wesselink, A. J. 1961, MNRAS, 122, 433
Gebhardt, K., Pryor, C., Williams, T. B., & Hesser, J. E. 1994, AJ, 107, 2067
Gebhardt, K., Pryor, C., Williams, T. B., Hesser, J. E., & Stetson, P. B. 1997, preprint
Geffert, M., Colin, J., Le Campion, J.-F., & Odenkirchen, M. 1993, AJ, 106, 168
Geisler, D. 1981, PASP, 96, 723
Gnedin, O. Y., & Ostriker, J. P. 1997, ApJ, 474, 223
Grillmair, C. J., Freeman, K. C., Irwin, M., & Quinn, P. J. 1995, AJ, 109, 2553
Grabhorn, R. P., Cohn, H. N., Lugger, P. M., & Murphy, B. W. 1992, ApJ, 392, 86
Guhathakurta, P., Yanny, B., Schneider, D. B., & Bahcall, J. 1996, AJ, 111, 267
Gunn, J. E., & Griffin, R. F. 1979, AJ, 84, 752
Hut, P., et al. 1992, PASP, 104, 981
Jaynes, E. T. 1983, Papers on Probability, Statistics, and Statistical Physics (Dordrecht: Reidel)
Jeffreys, H. 1961, Theory of Probability (Oxford: Clarendon)
King, I. R. 1966, AJ, 71, 64
King, I. R., Hedemann, E., Hodge, S. M., White, R. E. 1968, AJ, 73, 456
Kundić, T., & Ostriker, J. P. 1995, ApJ, 438, 702
Küstner, F. 1921, Veröff. Sternw. Bonn., No. 15
Larson, R. B. 1970, MNRAS, 150, 93
Lauer, T. R., et al. 1991, ApJ, 369, L45
Le Campion, J.-F., Colin, J., & Geffert, M. 1996, A&AS, 119, 307
Lugger, P. M., Cohn, H. N., & Grindlay, J. 1995, ApJ, 439, 191
Lupton, R., Gunn, J. E., & Griffin, R. F. 1987, AJ, 93, 1114
Mayor, M., et al. 1984, A&A, 134, 118
Meylan, G., Dubath, P., & Mayor, M. 1991, ApJ, 383, 587
Merritt, D., Meylan, G., & Mayor, M. 1997, AJ, 114, 1074
Oh, K. S., & Lin, D. N. C. 1992, ApJ, 365, 519
Okazaki, T., & Tosa, M. 1995, MNRAS, 274, 480
Peterson, R. C., Seitzer, P. O., & Cudworth, K. M. 1989, ApJ, 347, 251
Press, S. J. 1989, Bayesian Statistics: Principles, Models, and Applications (New York: Wiley)
Pryor, C., Latham, D., & Hazen, M. 1988, AJ, 96, 123
Pryor, C., & Meylan, G. 1993, in ASP Conf. Ser. 50, Structure and Dynamics of Globular Clusters, ed. S. G. Djorgovski & G. Meylan (San Francisco: ASP), 357
Saha, P., & Williams, T. B. 1994, AJ, 107, 1295
Sandage, A. 1970, ApJ, 162, 841
Scholtz, R.-D., Odenkirchen, M., Hinte, S., Irwin, M. J., Borgen, F., & Ziener, R. 1996, MNRAS, 278, 251
Sosin, C., & King, I. R. 1997, AJ, 113, 1328
Spitzer, L., & Chevalier, R. 1973, ApJ, 183, 565
Spitzer, L., & Shull, J. M. 1975, ApJ, 200, 339
Tonry, J. 1983, ApJ, 266, 58
Tonry, J., & Davis, M. 1979, AJ, 84, 1511
Weinberg, M. 1994, AJ, 108, 1398